Cerium conversion coating and sol-gel coating for corrosion protection of the WE43 Mg alloy

Gualter Silva Pereira [a], [b], *, Oscar Mauricio Prada Ramirez [c], **, Pedro Renato Tavares Avila [a], Julian Arnaldo Avila [d], [e], Haroldo Cavalcanti Pinto [a], Marcos Hideki Miyazaki [f], Hercílio Gomes de Melo [c], Waldek Wladimir Bose Filho [a]

[a] São Carlos School of Engineering, University of São Paulo, Department of Materials Engineering, Av. Joao Dagnone, 1100 Jd. Sta Angelina, 13563–120 São Carlos, SP, Brazil
[b] Federal Institute of São Paulo (IFSP), Av. Pastor Jose Dutra de Moraes, 239, 15808–305, Catanduva and Américo Ambrósio, 269, 14169–263- Jardim Canaa, Sertãozinho SP, Brazil
[c] Departamento de Eng. Metalúrgica e de Materiais-Escola Politécnica da Universidade de São Paulo, Av. Prof. Mello de Moraes, 2463 São Paulo, SP, Brazil
[d] Department of Strength of Materials and Structural Engineering, Barcelona School of Engineering (ETSEIB), Universitat Politècnica de Catalunya · BarcelonaTech (UPC), Avda. Diagonal 647, 08028 Barcelona, Spain
[e] São Paulo State University (UNESP), Campus of São João da Boa Vista, Av. Profª Isette Corrêa Fontão, 505, Jardim das Flores, 13876–750 São João da Boa Vista, SP, Brazil
[f] Embraer, 12227–901 São Jose Dos Campos, SP, Brazil

ARTICLE INFO

ABSTRACT

In this work, the electrochemical behavior and morphological characterization of a system consisting of a cerium conversion layer, a hybrid sol-gel coating, and the two coatings applied sequentially (duplex) have been evaluated for the corrosion protection of WE43 Mg alloy. The different characterization techniques showed that the surface coverage by the hybrid coating was improved by the previous application of the conversion coating. The fitting of the impedance diagrams with electrical equivalent circuits allowed to propose a physical model for the coating, evidencing its interaction with the porous Mg oxide/hydroxide layer. Self-healing properties of the duplex coating were also disclosed.

1. Introduction

Mg-based alloys are increasingly being considered for structural applications. Their low density coupled with their high specific mechanical strength render these materials ideal for automotive and aerospace structural applications, where weight reduction is constantly pursued. However, the large-scale application of these alloys is limited by their high corrosion susceptibility in different aggressive environments, especially in the presence of chlorides [1,2]. Recent studies have shown that the addition of rare-earth (RE) elements can improve the mechanical properties and the corrosion resistance of Mg alloys [3–11]. Among the RE-based Mg alloys, the non-flammable Mg WE43 (Mg-Y-Nd-Zr) has drawn the attention of several researchers [4,8,12–19]. Unfortunately, their corrosion resistance is much lower than that found in aluminum alloys currently chosen for light structural projects [8].

The corrosion resistance of Mg alloys can be improved by employing surface coatings, preventing their contact with the environment, and through the presence of some chemicals aiming for corrosion inhibition [20,21]. The benchmark for corrosion protection of most metals is based on carcinogenic chromate ions [2,22–25], which, besides providing good corrosion resistance properties also presents self-healing abilities. Nevertheless, environmental and health concerns have urged the replacement of such chemicals in the surface treatment industry. Among the proposed alternative methods, Ce-based conversion coatings seem to be particularly suited for reactive metals. The protective layer precipitates at sites of increased pH due to cathodic activity, thus blocking further electrochemical reactions [26,27]; therefore, intrinsic electrochemical activity is the driving force for the conversion layer precipitation.

Ce conversion coatings have been investigated for corrosion protection of different surface-active metals and alloys [28–32], including Mg

* Corresponding author at: São Carlos School of Engineering, University of São Paulo, Department of Materials Engineering, Av. Joao Dagnone, 1100 Jd. Sta Angelina, 13563–120 São Carlos, SP, Brazil.
** Corresponding author.
E-mail addresses: gualter@alumni.usp.br (G.S. Pereira), oscarmprada@gmail.com (O.M.P. Ramirez), julian.arnaldo.avila@upc.edu (J.A. Avila).

alloys [21,33]; however seldom they have been used to protect Mg-RE alloys [34,35]. Several works show that the top-view of the conversion layer completely covering the substrate is cracked, exhibiting a so-called dry mud appearance, which some authors claim to be composed of a bi-layered structure [36,37]. Besides microstructural characterization, several works are devoted to investigating corrosion resistance. Rudd et al. [34] reported that the conversion coating produced by immersion in Ce solution was beneficial in decreasing pure Mg and WE43 alloy dissolution in a pH 8.5 buffer solution; however, the coatings deteriorated after 10 h exposure to the test solution. Takenata et al. used weight loss measurements to evaluate the corrosion behavior of Mg with different amounts of added RE elements and further protected with RE conversion layers. They reported increased corrosion resistance irrespectively to the RE element (La, Nd, Ce) used in the conversion bath [35]. Montemor et al. [38] applied Ce conversion coatings based on different Ce salts to an AZ31 Mg substrate. The corrosion resistance evaluated using polarization curves revealed improved behavior for all coatings, at various degrees, depending on the anion associated with the Ce cation. However, as shown in many works [36,39,40], the increase in the corrosion resistance evaluated by EIS seldom exceeds one order of magnitude, indicating that further improvement is necessary. Nevertheless, as RE conversion coatings exhibit rough surface morphology, they can be used as a base support for top coatings, like paints and organic coatings [1].

Another alternative investigated to improve the corrosion resistance of Mg alloys are organosilanes and hybrid (organic-inorganic) coatings produced by the sol-gel technology. These coating systems offer significant advantages such as good adhesion to the substrate surface via chemical bonding, providing good adhesion between the substrate and organic paints, cost-effectiveness, low life-cycle environmental impact, and simple application procedures, which may be easily adapted by industry [1,21,22]. Many works are available in the literature, and, overall, promising results are reported. For example, Zhang et al. [41] reported that the corrosion resistance of AZ91D alloy in 0.6 M NaCl solution was improved by the surface treatment with a sol–gel-based CeO$_2$. In the work of Dalmoro et al. [42], a hybrid organophosphonic-silane coating was applied for corrosion protection of AZ91 Mg alloy submitted to different surface treatments. The authors reported improved performance of hybrid coating attributed to the multiple bonds formed among the constituents of the coating themselves and with the Mg-oxide/hydroxide inner layer. Lamaka et al. [43] observed that the tris (trimethylsilyl) phosphate-containing sol-gel coating conferred good corrosion protection to the AZ31B alloy in 0.005 M NaCl solution due to its chemical interaction with the magnesium substrate. Differently from the Ce-conversion coatings that precipitate on the substrate surface, chemical bonding between the hydrolyzed molecules and the substrate and between the hydrolyzed molecules themselves (crosslinking) within the coating structure are important for a good performance of the sol-gel layer. Therefore, as largely documented in the literature, the properties of organosilanes and hybrid coatings are highly dependent on the hydrolysis solution composition (amounts of precursors, pH, water content, hydrolysis time), as well as on the curing temperature and time and substrate pre-treatment; thus, coatings produced using the same precursors may present different anticorrosion performances according to their production protocols.

Concerning the interactions of the sol-gel layer with the substrate surface, several groups consider that they occur through hydrogen bonds (OH-OH interaction) and by the formation of metallosiloxane bonds (Me-O-Si) [22,44–48], which reaction is similar to condensation during polymer cross-linking. In this latter case, the coating becomes covalently bound to the surface, increasing its stability. Recently, Mrad et al. [48], using FTIR, evidenced the existence of Al-O-Si bonds for the Al substrate protected with a sol-gel coating, strongly supporting the formation of an intermediate layer between the substrate and the organosilane network, characterized by these covalent bonds.

Multi-step coating systems, combining conversion, anodization or either other surface modification techniques with sol-gel coatings could afford the best properties of each step, providing barrier protection as well as possible self-healing properties [1,49–53]. Bestetti et al. [49] observed that a sol-gel coatings on bare AM60B alloy in 0.6 M NaCl solution does not increase the corrosion resistance of the substrate; however, an anodic oxidation pretreatment enhanced the adhesion of the sol-gel layers and improved the corrosion protection. Tan et al. [50] reported that the addition of an intermediate porous anodized layer in a AZ91D alloy improved the adhesion of the subsequently applied sol-gel layer, reduced the porosity levels, and improved the corrosion resistance in 0.5 M NaCl solution. Gutiérrez et al. [1] found that the hybrid sol-gel film confers good corrosion protection to a Elektron21 alloy in 0.05 M NaCl solution; however, when an intermediate phosphate conversion layer was added, the corrosion resistance increased compared to the single sol–gel coating. An intermediate phosphate layer also enhanced the corrosion resistance of the AZ31B alloy. According to Khramov et al. [51], the improvement can be explained by the chemical binding of phosphonate groups to the metal surface resulting in enhanced hydrolytic stability of the formed P–O–Mg bonds. Pinto et al. [52] observed that the formation of a passive film and of an anodic layer, by themselves, have little protective performance on a WE54 alloy in 0.005 M NaCl solution. Still, when combined with a silane layer, a synergistic effect was evidenced. Nezamdoust et al. [53] observed that a cerium−vanadium conversion coating provided minimal protection against corrosion while the subsequently applied sol-gel significantly improved the corrosion resistance of the AM60B alloy. According to the authors, the sol-gel film improves the corrosion resistance by sealing cracks in the cerium-vanadium conversion coating and acting as a barrier film. Indeed, it is intuitive that increasing the interlocking of the sol-gel film with a porous and rough intermediate layer could improve the adhesion of the organic layer to the substrate. Although, as shown in this paragraph, multilayer approaches have been adopted to protect Mg alloys, to the best of the authors knowledge, no multilayer coating with characteristic similar to that used in the present investigation applied to Mg-RE alloys has been reported in the literature.

In this work, the morphology, composition, and anticorrosion properties of separately and combined systems, involving a Ce-based conversion film and a hybrid sol-gel coating, were studied to prevent the corrosion of a WE43 alloy in saline environments. The hybrid sol-gel composition was chosen aiming for future interaction with an epoxy coating applied in a complete protection system. Furthermore, the electrochemical tests and characterization procedures were designed to highlight both the general corrosion protection afforded by the proposed systems to the Mg substrate and their self-healing abilities, this latter by means of local electrochemical measurements.

2. Experimental procedure

2.1. Material

WE43C-T5 Mg alloy (referred to as WE43 hereafter), acquired from Magnesium Elektron N.A. Inc, was considered in this study. Its chemical composition is detailed in Table 1. The hot-rolled WE43 alloy is precipitation hardened without a prior solution treatment, according to the T5 condition [54].

Table 1
Chemical composition of the WE43 alloy from energy-dispersive X-ray spectroscopy (EDS) measurements.

Elements (wt%)	Mg	Y	Nd	Zr	Others
WE43	Bal.	2.7	1.6	0.2	0.13

2.2. Coatings preparation

The metallic samples were initially grounded using SiC sandpaper up to # 1200, rinsed with ethanol, and dried with a hot air stream. Then they were etched in HNO_3 20 g L^{-1} for 2 min at room temperature, rinsed with deionized water, ethanol and dried with hot air stream.

The Ce conversion layer (CeP coating) was obtained by immersion of the surface-treated magnesium substrates for 2 min in a 50 mM $Ce(NO_3)_3.6 H_2O$ + 10% v/v H_2O_2 aqueous solution at (50 ± 2) °C, similar to post-treatments previously used for corrosion protection of aluminum alloys [55–57].

The sol-gel solution was prepared as follow: the inorganic tetraethoxysilane (TEOS) (10%v/v) and organic (3-glycidoxypropyl) trimethoxysilane (GPTMS) (20%v/v) precursors were added together to a mixture of ethanol (10%v/v) and distilled water (60%v/v) under stirring and then the pH was adjusted with acetic acid in the range of 3.5–4. The solution was then stirred at room temperature for 2 h for hydrolysis to take place. For the hybrid (organic-inorganic) coating (Hyb) application, the magnesium substrate was immersed in the hydrolyzed solution and maintained for 2 min by a dip-coating process. The withdrawal rate was fixed at 10 cm min^{-1}. The samples were then cured at 150 °C for 1 h. In the hybrid coating structure, the full hydrolysis of the inorganic precursor (TEOS) results in a Si atom linked to four OH groups (silanol), whereas the full hydrolysis of the organic precursor (GPTMS) results in the central Si atom bound to three hydroxyl (silanol groups) and to the glycidoxypropyl group (not hydrolyzed), thus introducing an organic molecule in the coating structure. The hydrolyzed TEOS provides adhesion to the metallic substrate and high corrosion resistance [58], this latter due to the crosslinking of the silanol groups. However, its intrinsic inorganic nature introduces defects in the coating structure (it is brittle) and the curing temperature for cross-linking is too high to be used with Mg alloys [59]. These drawbacks are circumvented by the introduction of the organo-modified silane (GPTMS), which, besides enhanced flexibility, thus diminishing crack susceptibility [60], reduces the curing temperature, setting it below 150 °C [61], allowing obtaining a crack-free and dense coating.

The duplex coating (CeP-Hyb) was prepared by sequentially dipping the Mg samples in the conversion and in the hydrolyzed hybrid sol-gel solution, following the protocols previously described. A washing step was introduced between each step.

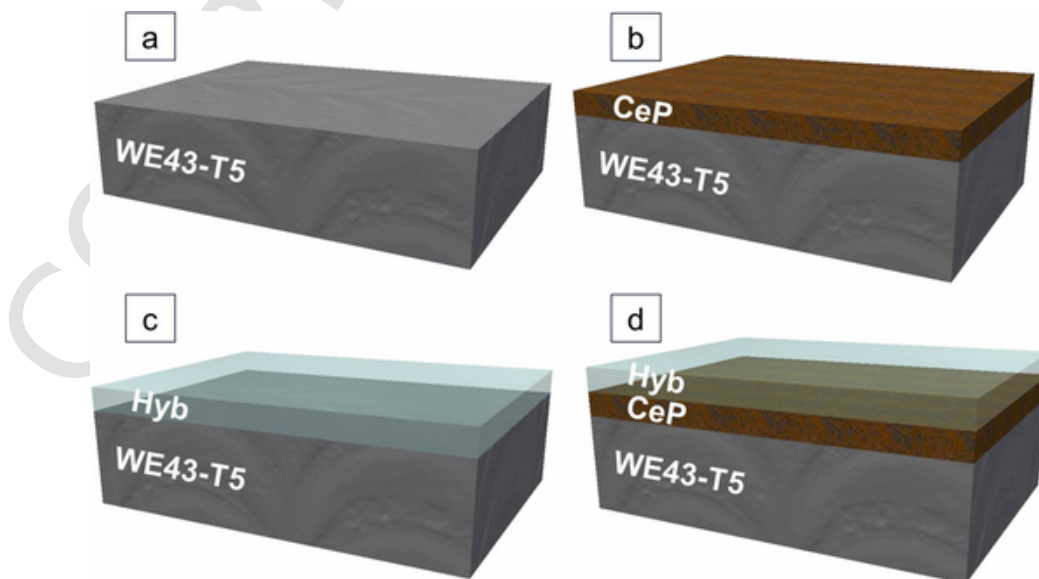The three coatings systems are schematically represented in Fig. 1.

2.3. Characterization of Ce and sol-gel films on WE43 alloy

Analysis of the microstructure was undertaken by optical microscopy (OM), using a Zeiss ™ model Stemi 2000-C, and by scanning electron microscopy (SEM), using a FEI® model FE-50 in secondary (SE) and backscattered electron (BSE) modes, as well as energy dispersive X-ray analysis (EDS).

The surface morphology and roughness of the bare and coated samples were investigated using a Nanosurf Flex Atomic Force Microscope in tapping mode on an area of (30 × 30) μm².

The wettability of bare WE43-T5 alloy and coated specimens was evaluated using the sessile drop method by static contact angle (θ) measurements with distilled water. For the experiments, a Dataphysics Contact angle System OCA was employed, using digital analysis software (Data physics SCA 20).

2.4. Electrochemical characterization

Electrochemical measurements were conducted in a conventional three-cell set-up, using a Gamry 600 + potentiostat. The working electrodes were the WE43 alloy with and without coatings. A Pt wire and Ag/AgCl were used as counter and reference electrode, respectively. The electrolyte was a 0.1 M NaCl solution. Electrochemical impedance spectroscopy (EIS) was performed up to 24 h of immersion, considering a perturbation amplitude of 10 mV$_{rms}$ around the open circuit potential (OCP), with a frequency range between 10^5 to 10^{-2} Hz. Diagrams were acquired regularly along the test period. The data treatment was performed with equivalent electric circuit (EEC) using the ZView software. Potentiodynamic polarization measurements were carried out as complement after 1 h and 24 h of immersion, from −200 mV against the OCP up to 10^{-3} A/cm², using 1 mV/s as scan rate in the anodic direction.

Local electrochemical impedance spectroscopy experiments in the mapping mode (LEIM) were carried out to investigate self-healing ability of the coatings. The experiments were performed using a commercial Ametek® VS-LEIS system, controlled by the VersaScan® software. The admittance (Ω^{-1}.cm^{-2}) maps were obtained at a single frequency of 50 Hz with a perturbation amplitude of 100 mV (rms) and step size of 200 μm. An artificial defect (3 mm long scratch) was performed at the surface of the Hyb and CeP-Hyb coated samples. The scanned area was 0.25 cm² and the experiments were performed in NaCl 5 mM solution

Fig. 1. Schematic representation of the WE43-T5 samples: (a) bare substrate, (b) cerium conversion coating (CeP), (c) hybrid sol-gel coating (Hyb), and (d) duplex CeP-Hyb coating.

using an Ag/AgCl (KCl satd) reference electrode and a Pt ring as counter electrode. The use of low concentrated solution increases the Ohmic drop, thus improving the acquired electrical signs, and also helps to preserve the coating, enhancing the response at the defective sites. The parameters used in these experiments were chosen according to the literature and the frequency used to acquire the admittance maps was set at a value that can provide information about the self-healing effect of the Ce inhibitor [62], without extending the duration of the experiment.

3. Results and discussion

3.1. Morphological and compositional characterization of coatings

OM images of the samples after preparation showed that the CeP coating (Fig. S1(a)-Supplementary material) presented a yellow hue, typical of Ce conversion coatings [63]. Concerning the samples protected with the hybrid coating: Hyb and CeP-Hyb, the former exhibited several defects along the surface, characterized as whitish stains (Fig. S1(b)-Supplementary material), whereas the latter was more homogeneous with no visible signs of defects at the selected magnification (Fig. S1(c)-Supplementary material). Fig. 2 shows the SEM micrographs and EDS characterization of the bare WE43 sample and with the different coatings. The surface morphology of the WE43 alloy, shown in Fig. 2a, is uniform, but some fine nicks resulting from the grinding process are still visible, the EDS analysis, Fig. 2b, shows the chemical composition of the WE43 alloy. The Ce conversion coating, shown in Fig. 2c, uniformly covers the alloy surface with a featureless deposit which can be encountered in Ce conversion coatings formed for short periods [33]; however, at higher magnification (Fig. 2d), it is possible to observe the dry mud morphology characteristic of this type of coating [36,37, 63–65]. The EDS analysis in Fig. 2e, besides the main alloying elements, Mg, Y, Zr, and Nd, shows a high concentration of Ce, confirming its deposition in the alloy surface. As shown in Fig. 2f, the sol-gel process obtains an almost homogeneous, integrated, uniform, and crack-free coating. However, it is possible to observe circular defects, possibly arising from hydrogen gas production during the sample immersion in the acidic hydrolysis solution (Fig. S2a - Supplementary material). Gutierrez et al. [1] have found that hydrogen gas production during Mg alloy immersion in the sol solution leads to the formation of defects in the sol-gel film. Nezamdoust et al. [66] attributed the defects observed in sol-gel coatings to the reactivity of the Mg alloy substrate concerning the sol solution, this feature is evidenced in the high magnification SEM image (Fig. 2g) at which a rough surface of the base alloy is observed. The EDS analysis in Fig. 2h shows the presence of Si, confirming the hybrid deposition on the WE43 alloy surface. Fig. 2i and j show the surface of the sample with the CeP-Hyb coating. The lower magnification micrograph (Fig. 2i) indicates that the surface is more uniform (less rough) than the CeP sample. However, the enlarged image (Fig. 2j) demonstrates that the aspect of dry mud associated with the Ce conversion layers persists, which was an expected outcome as the conversion layer was formed previously; this result also indicates that this typical feature is not resultant from the vacuum in the SEM chamber. Finally, no bubbles were observed on the Ce-coated sample during its immersion in the hybrid solution (Fig. S2b in Supplementary material), thus, defects associated with this phenomenon were not observed in the CeP-Hyb coating. The EDS results present C, O, Mg, Y, Nd, Zr, Si, and Ce (Fig. 2k), confirming the integration of the coating elements on the sample surface. However, the weight percentages of Si and Ce are nearly equivalent to the individual coatings (Fig. 2e and h), indicating that the combined coating completely and homogeneously covers the WE43 alloy substrate; moreover, an important reduction in the Mg content was verified (compare Fig. 2e, h and k), indicating the presence of a thicker duplex top layer on the sample surface.

Cross-sectional SEM images of the different coatings are depicted in Fig. 3. The CeP coating (Fig. 3a), which EDS analysis (not presented) showed to be composed of Ce oxides, presented some defects, in accordance with its surface image (Fig. 2b and c). For the Hyb sample (Fig. 3b), a Si-rich homogeneous layer was identified. Finally, the CeP-Hyb coating (Fig. 3c) presented Si and Ce along its whole thickness (verified by EDS), indicating percolation of the hybrid solution through the cerium conversion coating cracks. As indicated in the Figures, the thicknesses of the coatings were estimated as: 0.18 ± 0.01 μm (CeP), 1.65 ± 0.09 μm (Hyb) and 2.06 ± 0.05 μm (CeP-Hyb). For the sample CeP-Hyb (Fig. 3c) is possible to see the cracked Ce conversion coating (white layer) underneath the hybrid sol-gel coating.

3.2. Contact angle measurements

The hydrophobicity of the coatings was investigated using contact angle measurements. Yao et al. [67] reported that for all aqueous solutions, independently of pH, Mg alloys are hydrophilic, with a contact angle lower than 90°, i.e., aggressive aqueous solutions can easily spread over the Mg surface corroding the substrate.

Fig. 4 displays the contact angles for the bare sample and for those protected with the three coatings. The uncoated substrate exhibits a contact angle of ~60° (Fig. 4a), close to those reported in the literature for WE43 alloy [68,69]. The CeP sample (Fig. 4b) showed the smallest contact angle (about 27°), which is similar to other findings in the literature for Ce conversion coatings in Mg alloys [63,70] and must be related to the cracks evident in the dry-mud morphology of the Ce-conversion coating observed in the SEM images of Fig. 2b,c. In addition, Ce oxides and hydroxides provide increased hydrophilicity and wettability of the substrate, similar to what has been reported for AZ31 alloy protected with Ce-based conversion coatings [70]. The Hyb and CeP-Hyb samples (Fig. 4c and d) presented higher contact angle values, close to 85° and 89°, respectively, suggesting a more hydrophobic surface arising from the presence of organic chains in these coatings' compositions. Overall, the results indicate that, no matter the coating procedure, the surface remains hydrophilic; nevertheless, the presence of the hybrid coating substantially decreases the interactions of the surface with the water droplet compared to the CeP coating. It must also be considered that the high wettability of the CeP sample may contribute to adhesion improvement between the conversion coating and the hybrid sol-gel coating [71].

3.3. AFM

Fig. 5 displays the AFM surface maps obtained using the tapping mode. The bare WE43-T5 alloy (Fig. 5a) shows only marks from the grinding process. In contrast, the CeP sample (Fig. 5b) exhibits a very rough surface with morphological features that must result from the cracks observed in the SEM analysis (See Fig. 2b). The Hyb sample (Fig. 5c), on the other hand, shows a regular and smooth surface, indicating complete coverage of the substrate; however, the AFM image evidences the presence of some round-shaped defects, which, as aforementioned, may result from the hydrogen bubbles evolved during the coating application procedure, as observed in Fig. S2a in Supplementary material. Finally, the CeP-Hyb coating (Fig. 5d) presents no surface defects and the hybrid coating seems to completely cover the substrate. Nevertheless, it shows wavy patterns, which must arise from the coverage of the rough underlying Ce conversion coating.

Evaluation of the surface roughness of the different samples by means of arithmetic roughness (Ra) and root mean square roughness (Rrms): WE43-T5, Ra = 154 nm and Rrms = 189 nm; CeP, Ra = 241 nm and Rrms = 366 nm; Hyb, Ra = 25 nm and Rrms = 63 nm; and CeP-Hyb, Ra = 81 nm and Rrms = 115 nm, confirmed the overall analysis of the AFM images. Similar to previous works with Ce conversion coatings [72], it is evident that there is an in-
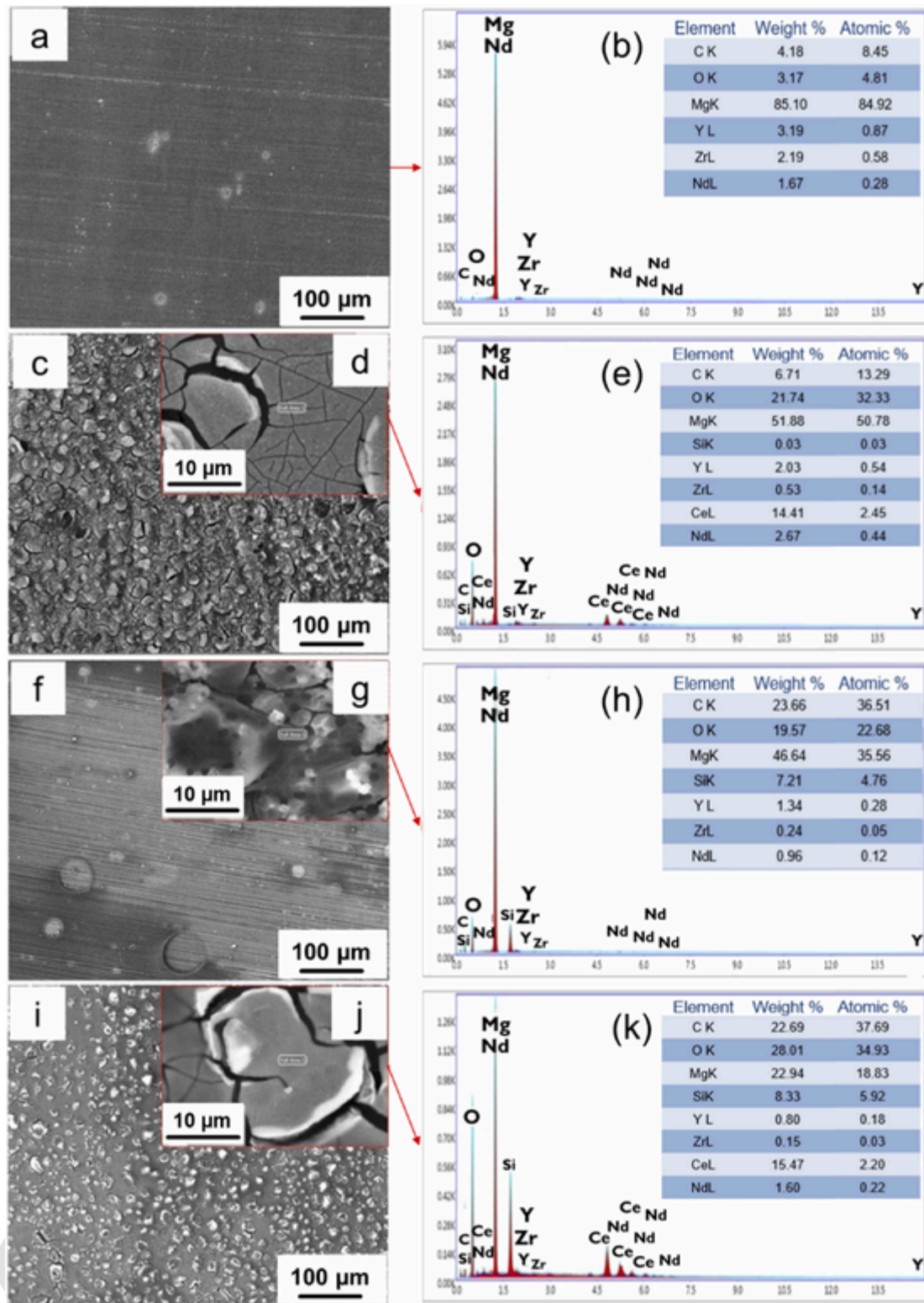
Fig. 2. SEM micrographs of: (a) bare substrate, (c-d) cerium conversion coating (CeP), (f-g) hybrid sol-gel coating (Hyb) and (i-j) duplex CeP-Hyb coating on WE43-T5 substrates and EDS analyses of (b) bare substrate, (e) CeP, (h) Hyb and (k) CeP-Hyb coating.

crease in the roughness with the deposition of the CeP coating when compared to the WE43-T5 substrate; moreover, the Hyb coating presents the lowest roughness condition. Conversely, the application of the CeP-Hyb treatment showed an intermediary condition between the other two coatings, which is coherent with the coverage of the rough CeP conversion layer by the smooth hybrid layer.

3.4. Corrosion resistance evaluation

3.4.1. Potentiodynamic polarization

Fig. 6 presents the potentiodynamic polarization curves acquired after 1 h (a) and 24 h (b) of immersion in the test electrolyte. For both immersion times and for all samples, the cathodic branches show an acti-
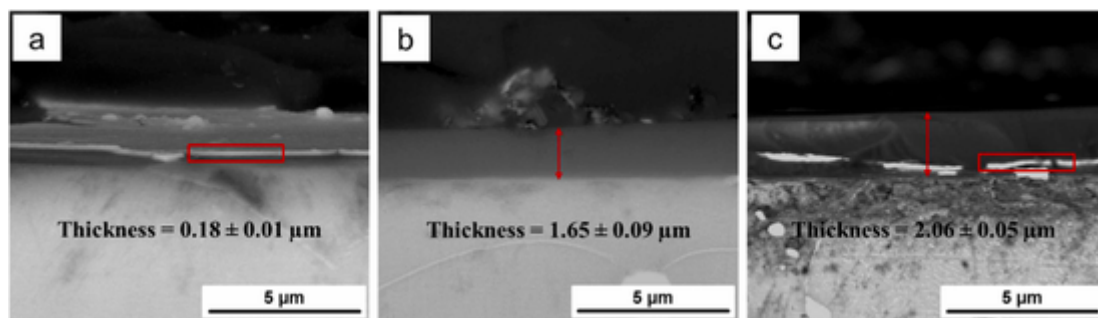
Fig. 3. Cross-sectional SEM micrographs of the different coatings: (a) CeP, (b) Hyb and (c) CeP-Hyb.
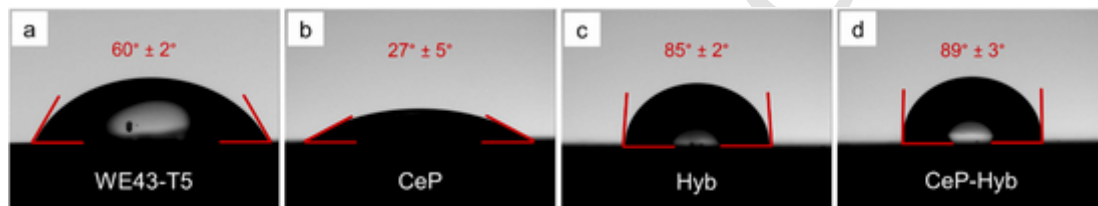

Fig. 4. Water contact angle measurements for (a) bare substrate, (b) cerium conversion coating (CeP), (c) hybrid sol-gel coating (Hyb), and (d) duplex CeP-Hyb coating on WE43-T5 substrates.
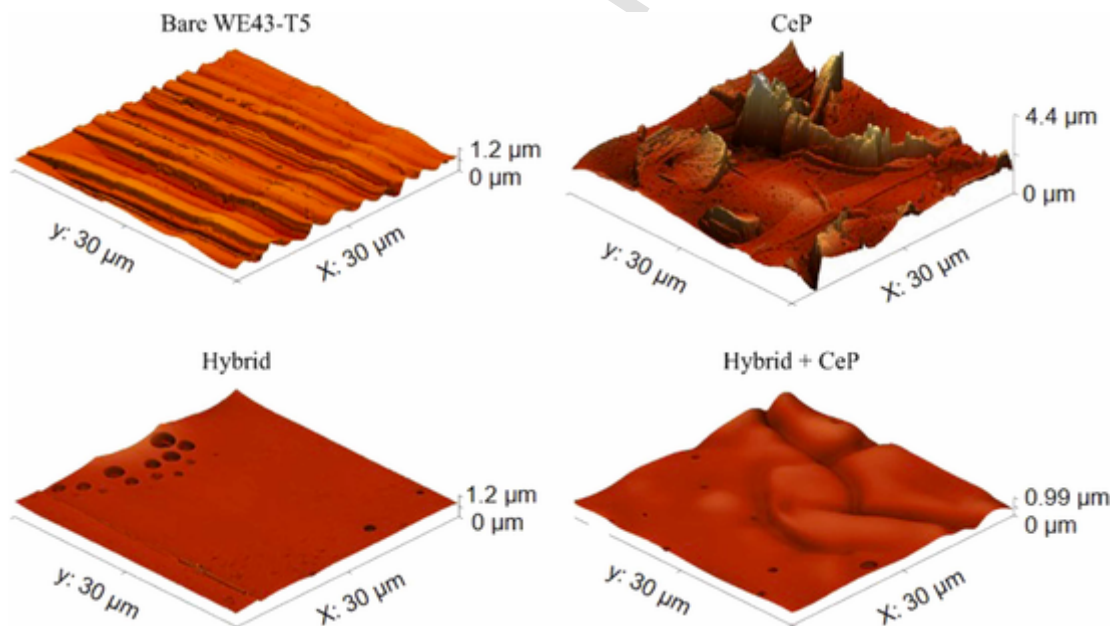

Fig. 5. AFM maps of the bare WE43-T5 (a); CeP (b); Hyb (c); and CeP-Hyb (d) sample.

vation-controlled process due to the reduction of H^+ ions [73]. Regarding the anodic behavior, except for the bare sample, that displays an activation-controlled process for short immersion times, all samples show passive responses, which, nevertheless, are not characterized by a well-defined passive current.

To perform a more accurate analysis of the polarization behavior of the different samples, parameters extracted from these experiments are summarized in Table 2. In this table, i_{corr} was determined from the extrapolation of the cathodic branch, whereas, the current densities under polarized conditions ($E_{corr}+50$ mV and E_{corr}-50 mV) were determined as an effective way to compare the response of the different samples when displaced from the stationary condition characterizing the corrosion potential [74]. The analysis of the results for the coated samples shows that E_{corr} is similar at each immersion time and increases with increased exposure to the electrolyte. On the other hand, E_{corr} for the bare sample decreases with immersion time: it is more positive than the

coated samples after 1 h and more negative after 24 h immersion. The different behavior for this latter sample can be explained based on both the i_{corr} value and the polarization behavior. As shown in Table 2, after 24 h exposure, i_{corr} increases. Similarly, both the anodic and cathodic branches of the polarization curves undergo depolarization ("i" at $E_{corr}+50$ mV and E_{corr}-50 mV increase in modulus), indicating increased corrosion activity for the bare sample. Interestingly, the current density at $E_{corr}+50$ mV is higher for the sample exposed during 24 h, even though a passivating range could be observed in this curve, indicating that the magnesium hydroxide layer formed when Mg alloys are exposed to different electrolytes is not very protective, as reported by several authors [75–78].

For the coated samples, i_{corr} and both the anodic and cathodic current densities away 50 mV from E_{corr} slightly decrease with immersion time, indicating enhanced corrosion resistance. This behavior can be ascribed to the precipitation of corrosion products at the defective sites of
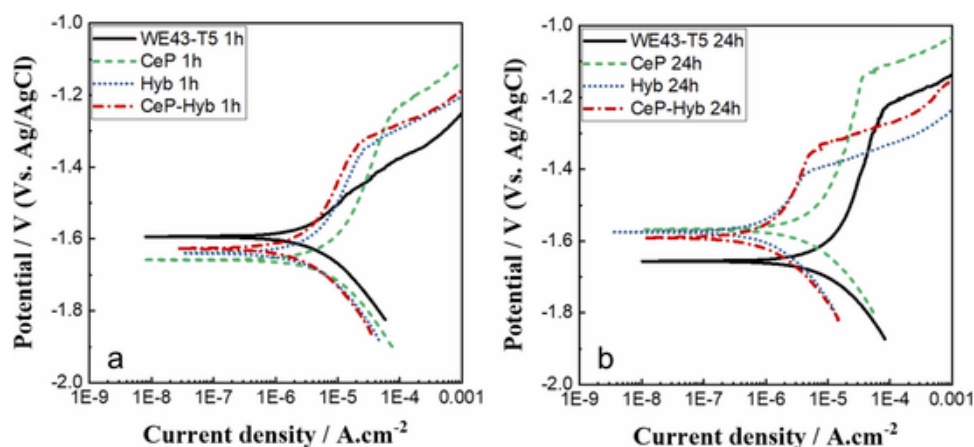
Fig. 6. Potentiodynamic polarization curves for the bare substrate, cerium conversion (CeP), hybrid sol-gel (Hyb) and duplex cerium-hybrid (CeP-Hyb) coating in NaCl 0.1 M after (a) 1 h and (b) 24 h. Scan rate 1 mV S^{-1}.

Table 2
Electrochemical parameters extracted from the potentiodynamic polarization curves with and without the different coatings after 1 h and 24 h of immersion in NaCl 0.1 M.

1 h						
Sample	E_{corr} [V vs Ag/AgCl]	i_{corr} [μA.cm^{-2}]	i_{ocp+50} mV [μA.cm^{-2}]	i_{ocp-50} mV [μA.cm^{-2}]	E_{pit} [V]	Prot. range [V]
WE43-T5	-1.59	2.8	17.8	- 17.6	–	–
CeP	-1.66	3.4	22.3	- 27.0	-1.24	0.42
Hyb	-1.64	1.1	12.6	- 15.8	-1.35	0.29
CeP-Hyb	-1.65	0.7	5.3	- 9.4	-1.33	0.32
24 h						
Sample	E_{corr} [V vs Ag/AgCl]	i_{corr} [μA.cm^{-2}]	i_{ocp+50} mV [μA.cm^{-2}]	i_{ocp-50} mV [μA.cm^{-2}]	E_{pit} [V]	Prot. range [V]
WE43-T5	-1.66	10.9	26.8	- 36.7	-1.23	0.43
CeP	-1.57	3.0	16.3	- 20.9	-1.14	0.43
Hyb	-1.57	0.8	4.7	- 5.1	-1.41	0.16
CeP-Hyb	-1.59	0.6	4.2	- 4.9	-1.35	0.24

the different coating systems, which may result from the precipitation of both Ce oxy-hydroxides (CeP coatings) and Mg(OH)$_2$. Based on these criteria: i_{corr} and current densities under polarized conditions, the protective ranking can be established as CeP-Hyb > Hyb > CeP at both immersion times. These results point to more effective protection afforded by the duplex system, indicating a synergistic effect between the two treatments.

Except for the bare alloy after 1 h immersion, all polarization curves exhibit a passive range and a breakdown potential (Epit). This latter is reported in Table 2 together with the corresponding passive range (Epit – E_{corr}) for each condition. It can be verified that, even though presenting lower i_{corr} and more polarized response under anodic polarization, the passive ranges for the samples Hyb and CeP-Hyb are smaller than for the CeP sample (after 1 h and 24 h immersion) and for the bare alloy (24 h); in addition, they decrease with immersion time. It is well known that under anodic polarization conditions, Mg alloys exhibit an unusual evolution of hydrogen gas denominated negative difference effect (NDE) [73,75,79,80], and according to experimental findings, the amount of evolved hydrogen increases for increased anodic polarization of the samples [80]. Even though no accordance exists about the mechanism behind the H$_2$ evolution process [73,79], it is clear that it involves H$_2$O either by means of a chemical [75,80] or electrochemical [73] reaction. The protective efficiency of polymeric coatings dramati-

cally relies on their adhesion to the metallic surface; it has been reported that if the rate of hydrogen generation at the coating-metal interface is faster than its removal by diffusion through the coating, a blister will form [81]; therefore, the increased amount of hydrogen gas generated upon anodic polarization of the samples (NDE effect) during the potentiodynamic experiments may develop blisters underneath the hybrid coating leading to their early failure when compared, for instance, with the CeP coating. On the other hand, considering the effect of immersion time on the breakdown potential, it is likely that with increased immersion time, the coatings will be more soaked with water molecules which will be more readily available for the NDE mechanism, thus decreasing the breakdown potential.

3.4.2. EIS tests

The evolution of the EIS responses during 24 h exposure to the test electrolyte for the whole set of samples is displayed in Fig. 7. For all of them, the Nyquist plots (Fig. 7(a, c, e, g)) are composed of two capacitive loops followed by a low frequency (LF) inductive loop. This EIS diagrams shape is often reported for Mg alloys in different electrolytes [75, 82–85], and the origin of the different time constants will be discussed later. Even though similar, a closer examination of the phase angle plots (Fig. 7(b, d, f, h)) for short immersion times (1 h) shows a displacement of the HF phase angle to higher frequencies for the Hyb and CeP-Hyb coated samples, that might reflect the presence of the hybrid layer.

The Nyquist plots displayed in Fig. 7 show similar evolution of the impedance moduli, characterized by an initial increase, up to 12–18 h, followed by an almost stable behavior and a slight decrease for the most prolonged immersion periods; however, the magnitudes were variable according to the analyzed sample (see Fig. 10). The characteristic frequencies of the inductive loops decrease with immersion time; therefore, they become less defined for more extended test periods indicating slower kinetics. For the bare sample, as reported by different authors, the initial increase of the impedance modulus might be ascribed to the thickening of the oxide layer [85,86], whereas the onset of localized corrosion may explain the deterioration of the corrosion resistance [85]. The diagrams also show that during the whole test period, there was no change in the shapes of the Nyquist diagrams (Fig. 7(a, c, e, g)), indicating that there is no variation in the corrosion mechanism; however, a close look in the phase angle diagrams (Fig. 7(f, h)) shows that, for the samples coated with the hybrid coatings (Hyb and CeP-Hyb), there is a shift of the high-frequency phase angle to lower frequencies with immersion time, which is not verified for the other two samples. This feature indicates a progressive water uptake by the hybrid coating layer, and will be further explored in the proposition of the physical model for the electric equivalent circuit (EEC) fitting procedure.
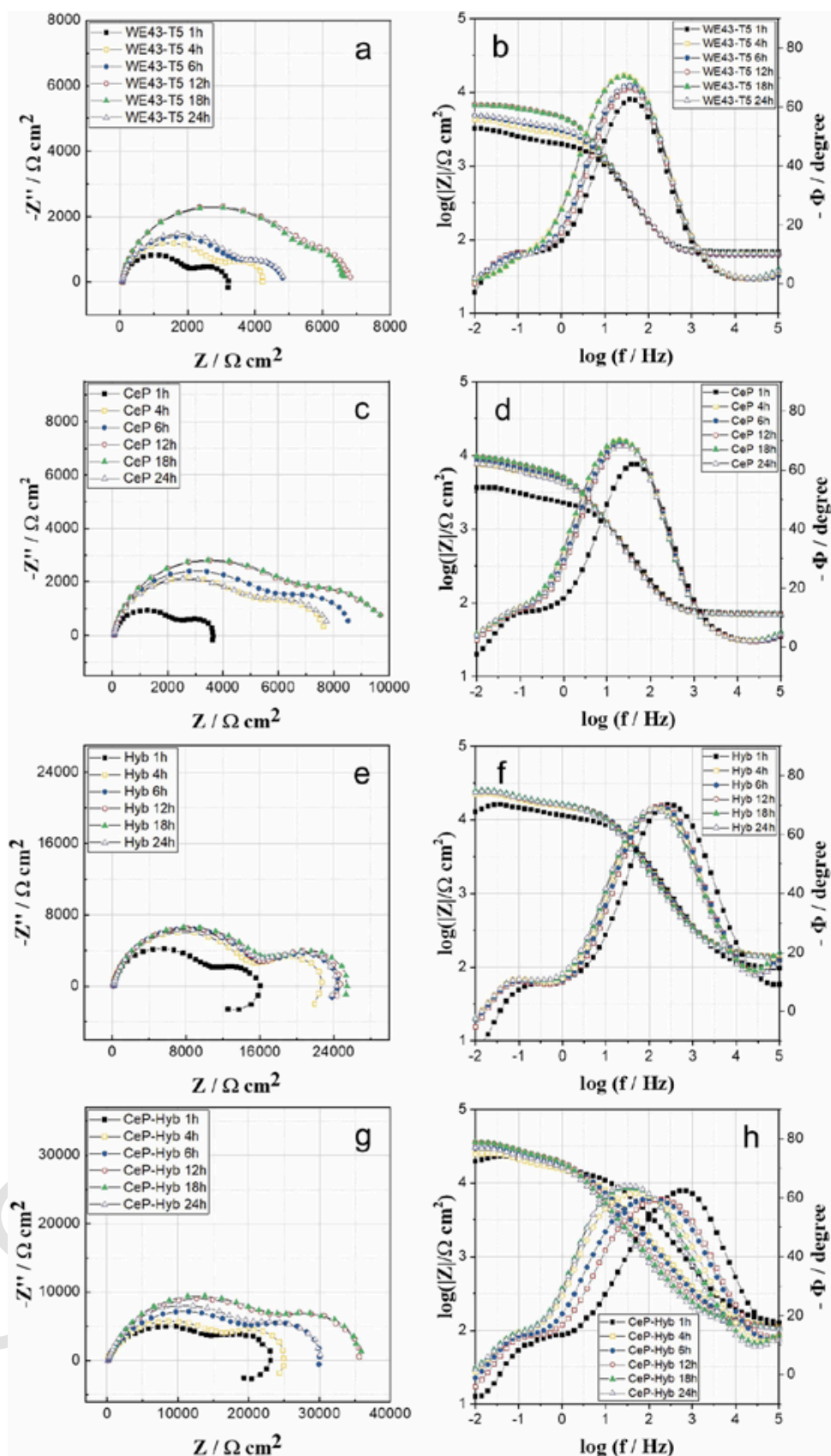
Fig. 7. Nyquist (a, c, e, g) and Bode (b, d, f, h) plots during 24 h immersion in NaCl 0.1 M of (a,b) WE43-T5, (c,d) CeP, (e,f) Hyb, (g,h) Cep-Hyb sample.

The diagrams in Fig. 7 show that, for the tested period, the samples submitted to any protection treatment display higher impedance modulus than the bare one, indicating increased corrosion resistance. After 24 h of immersion, when the inductive loop is no longer detected for any of the samples, the LF impedance modulus for the WE43-T5, CeP, Hyb, CeP-Hyb were, respectively: 4.82×10^3 Ohm.cm^2, 7.74×10^3 Ohm.cm^2, 2.38×10^4 Ohm.cm^2, 3.01×10^4 Ohm.cm^2. These values show the same corrosion resistance order as that identified in the polarization curves by means of i_{corr} determination.

For further comprehension of the corrosion behavior of the different samples, the impedance data were fitted using EEC. As mentioned and documented by Wang et al. [84], different EEC has been proposed in the literature to interpret the EIS responses of Mg and its alloys in several media. Besides differences in the arrangement of the EEC passive elements (parallel or series), different physical processes have been associated with each time constant (TC) of the EIS diagrams, even though most of them present similar shapes to those found in the present investigation. In the circuits, quite often, the capacitances are replaced by constant phase elements (CPE) to take into account the distributed behavior of the time constants.

Fig. 8 displays the EEC used to fit the whole set of experimental data, together with the physical model for the bare substrate. It is similar to the model employed by Baril et al. for the corrosion of pure Mg in sodium sulfate solution [75], with the difference that the capacitances were replaced by CPE. Baril et al. [75] proposed that the high frequency (HF) TC corresponds to a parallel association of two capacitances: one associated with the double layer (Cdl) and the other to a thin film capacitance (Cf) and two resistances: a film resistance (Rf), ascribed to a thin protective film, and the charge transfer resistance (Rct), ascribed to electrochemical reactions occurring at defective sites of the oxide film. According to their reasoning [75], Rf is too high

when compared to Rct and, therefore, no current leaks through this pathway, leading to its representation with dotted lines in the proposed EEC; in addition, as corrosion occurs through small defectives sites in the thin protective oxide film, this results in small capacitance values for the double layer due to reduced exposed area effect. The shape of the diagrams and the number of TC do not change with the application of the different protection systems, showing that the EIS measurements could not separate the response of the Mg oxide layer from that of the different coatings. This feature will be further explored in the analysis of the fitting results and in proposing a physical model for the coated samples.

The second capacitive loop of the EIS diagrams is ascribed to the diffusion of Mg ions within a bulk phase [82,83,87], and was fitted with a Warburg component associated with a diffusion process of finite thickness (Ws). The low frequency (LF) inductive loop was not fitted with the EEC of Fig. 8; initially, due to the small number of experimental points for its definition in most of the experimental diagrams, and secondly, due to the difficulties in associating the values extracted from the EEC fitting procedure to the physical-chemical phenomenon it represents. Following EIS diagrams interpretation for other metals [88,89], this LF inductive loop has been more frequently associated with relaxation of reaction intermediates [84], even though phenomena related to the breakdown of protective films have also been claimed to produce this inductive response [84,90,91]. Fig. 9 shows the experimental and fitted results for selected diagrams, at which the LF points associated with the inductive loops were deleted. The adequacy of the proposed model can be ascertained not only by the close similarity between the experimental and fitted data, but also by the low values of the errors associated with the fitted parameters (< 8 %) and with the chi-squared values (< 0.002).
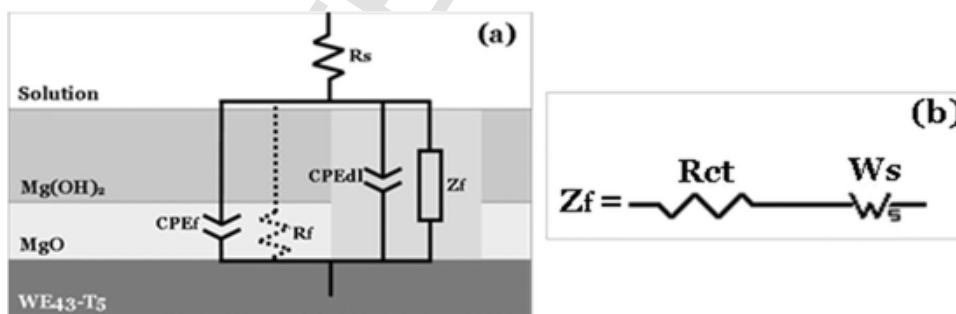

Fig. 8. (a) Electrical equivalent circuit (EEC) used to fit the EIS diagrams in NaCl 0.1 M of WE43-T5 alloy adapted from the model proposed by Baril et al. [75]; (b) Zf as used to fit the experimental data. In the EEC model the pathway through Rf is represented by a dotted line to indicate that no current leaks through this circuit element (Rf > > Rct).
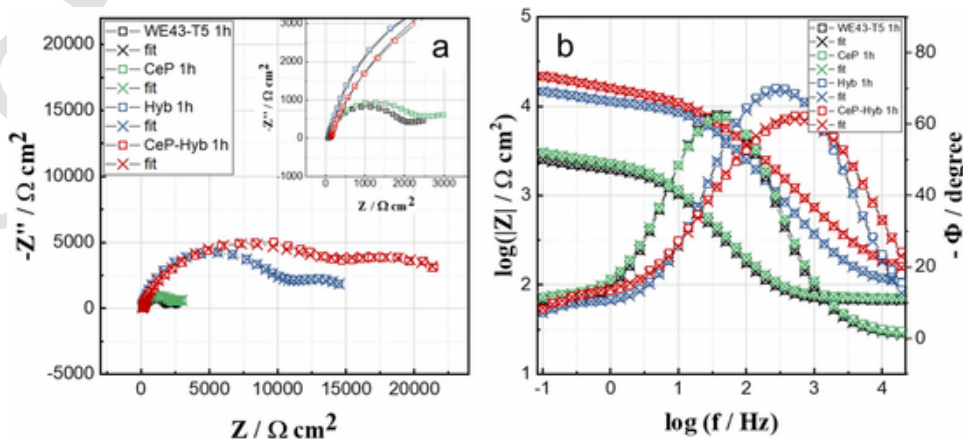

Fig. 9. Experimental (symbols) and fitted (crosses) diagrams for the different samples after 1 h immersion in NaCl 0.1 M: (a) Nyquist and (b) phase angle plots. The same color pattern was maintained for experimental and fitted data for each surface condition. The LF inductive loop was not considered for the fitting procedure.
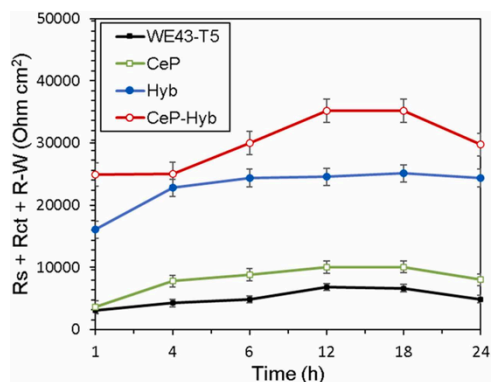
Fig. 10. Evolution of the sum of the resistive elements with immersion time obtained by the fitting procedure of the EIS diagrams.

Table 3 displays the variation of the passive elements of the EEC with immersion time. Initially, the high frequency (HF) resistance practically doubled for the Hyb and CeP-Hyb samples compared to WE43-T5 and CeP. For these two latter samples, as usual, this HF resistive element corresponds to the electrolyte resistance (R_s), as indicated in the EEC of Figs. 8a and 12a. On the other hand, for the Hyb and CeP-Hyb samples, before reaching the reactive regions of the electrode surface the electrolyte must penetrate through the defective sites (pores) of the hybrid coatings (R_H), which is in series with R_s (see physical models in Fig. 12 (b) and (c)); therefore, in these cases, the HF resistive element corresponds to the sum of two resistive elements in series; considering that R_s must be similar to the values obtained for the WE43-T5 and CeP samples, the low value of R_H indicates that conductive pathways with low resistance are established through the hybrid layer. The resistance associated with the HF capacitive loop, Rct, for all samples, initially increases (up to 18 h), which might reflect the precipitation of protective corrosion products. However, comparing the samples without (WE43-T5 and CeP) and with the hybrid coating (Hyb and CeP-Hyb), Rct for these two latter samples are roughly four times higher, indicating the precipitation of corrosion products with better barrier properties, as suggested by Hernández-Barrios et al. [92], and/or the reduction of the exposed area of unprotected Mg due to the presence of the hybrid coating.

The values of CPE-F for the WE43-T5 and CeP samples were about one order of magnitude higher than those associated with the Hyb and CeP-Hyb samples, indicating that the protective layer is thinner and/or more permeable to water molecules ingress. Regarding the variation of this parameter, it remains practically constant for the bare WE43-T5 sample and is slightly higher and with an increasing tendency for the CeP sample. This is likely due to the hydrophilic nature of the Ce precipitate [63,70,92], contributing to increased interaction with water molecules (see also results of the contact angle measurements Fig. 4b). For the hybrid coated samples, a steady increase of the capacitance is verified, indicating progressive water ingress, which agrees with the displacement of the HF phase angle to lower frequencies with immersion time (Fig. 7). Interestingly, even though thicker (Fig. 3c) and presenting the highest values associated with Rct, the CPE of the CeP-Hyb coating increases at a faster rate than in the Hyb coating, indicating easier water ingress, which might be a consequence of the presence of hydrophilic Ce precipitates in this protection system. The fitting results for the HF capacitive loop also show that, as the structure of the protective system becomes more complex, the CPE exponent (n) moves away from the ideal unit value. Hence, a normal distribution of time constants within the coating thickness can be associated, as suggested by Hirschorn et al. [93], an argument that has been recently used by Prada-Ramirez et al. [55–57] to explain the impedance response of anodized Al as sealing occurs within the pores. It is important to emphasize that, as extensively discussed in the literature, the oxide layer on

top of the Mg surface exposed to different electrolytes is composed of a porous, non-protective layer, mainly Mg(OH)$_2$, on top of a thin MgO compact and protective layer [75,83,84]. The percolation of the hybrid solution within the structure of the porous layer followed by its drying during the curing step must explain the relatively low "n" values for the Hyb sample; moreover, as shown in Table 3," n" becomes even lower for the CeP-Hyb sample, in this case, the hybrid layer must also percolate through the dry mud structure of the Ce conversion layer, leading to an even more complex behavior.

Finally, the passive elements associated with the diffusion of Mg within the bulk porous layer and/or the different coating systems are represented by the diffusion resistance (R-W) and the exponent associated with the Warburg impedance (n-W). The values for "n" lie within the 0.4–0.6 limit, indicating a fair agreement with a diffusion-controlled process. On the other hand, the resistance associated with the diffusion process (R-W) increases up to 12 h, related to the precipitation of protective corrosion products. Then, as the different systems deteriorate with immersion time, it starts to decrease.

Fig. 10 depicts the variation of the sum of the resistive elements of Table 3 (Rs + (R_H) + Rct + Rw), that can be directly associated with the resistance against the corrosion process, with immersion time. The patterns displayed in the plot are the same for all samples: an initial increase, followed by a stabilization plateau and finally a slight decrease. It shows that the overall resistance increases up to approximately 12 h, followed by a plateau, indicating stabilization of the corrosion process, and a final decline for 24 h of immersion; further, all coated samples present higher values in comparison with the bare substrate, although at different degrees. Particularly, the CeP-Hyb sample exhibits higher resistance values all along the test duration, which is in full agreement with the potentiodynamic polarization curves, which were acquired at the limits of the displayed time spam. Moreover, at the end of the exposure period the resistance associated with this sample is almost one order of magnitude higher than the bare sample, showing its effectiveness as a corrosion protection system.

3.5. Morphological and compositional characterization of the samples after the EIS experiments

After the completion of the EIS experiments, SEM micrographs of the corroded surfaces of the bare and coated substrates were taken, as shown in Fig. 11. Fig. 11a and b depict the bare substrate; from the lower magnification image, one observes a relatively uniform corrosion attack (Fig. 11a), whereas the higher magnification image (Fig. 11b) shows a cracked structure, that can be associated with Mg(OH)$_2$, that might indicate preferential sites for the onset of local attack. A large amount of oxygen was detected in the EDS analysis performed at this latter region (Fig. 11c), indicating the formation of a thick corrosion product layer. The EDS analysis shown in Fig. 11c also suggests incorporation of RE elements in the oxide layer composition, which might explain the superior corrosion resistance of this alloy compared to others submitted to even less aggressive solutions [43,87,94]. Previous studies have also attributed the more uniform corrosion of the WE43 alloy to the reduction of internal microgalvanic corrosion. This behavior can be explained by the similar electrode potentials between the Mg matrix (Mg, −2.37 V) and the alloying elements (Y: −2.37 V, Nd: −2.44 V), and more homogeneous microstructure and fine anodic precipitates well distributed in the matrix [95].

Fig. 11d depicts the surface morphology of the CeP sample after the EIS tests. The corroded surface exhibits a cracked structure very similar to that presented by the Hyb sample (Fig. 11g), indicating that, in this latter sample, it might have been originated from the corrosion of the alloy substrate, as no Ce is present in it. The morphology in Fig. 11d is also similar to the schematic representation of Leleu et al. [83] for the Mg(OH)$_2$ porous layer formed on an Mg-RE alloy and has also been reported for other RE-modified Mg alloys in different media [68,96]. On
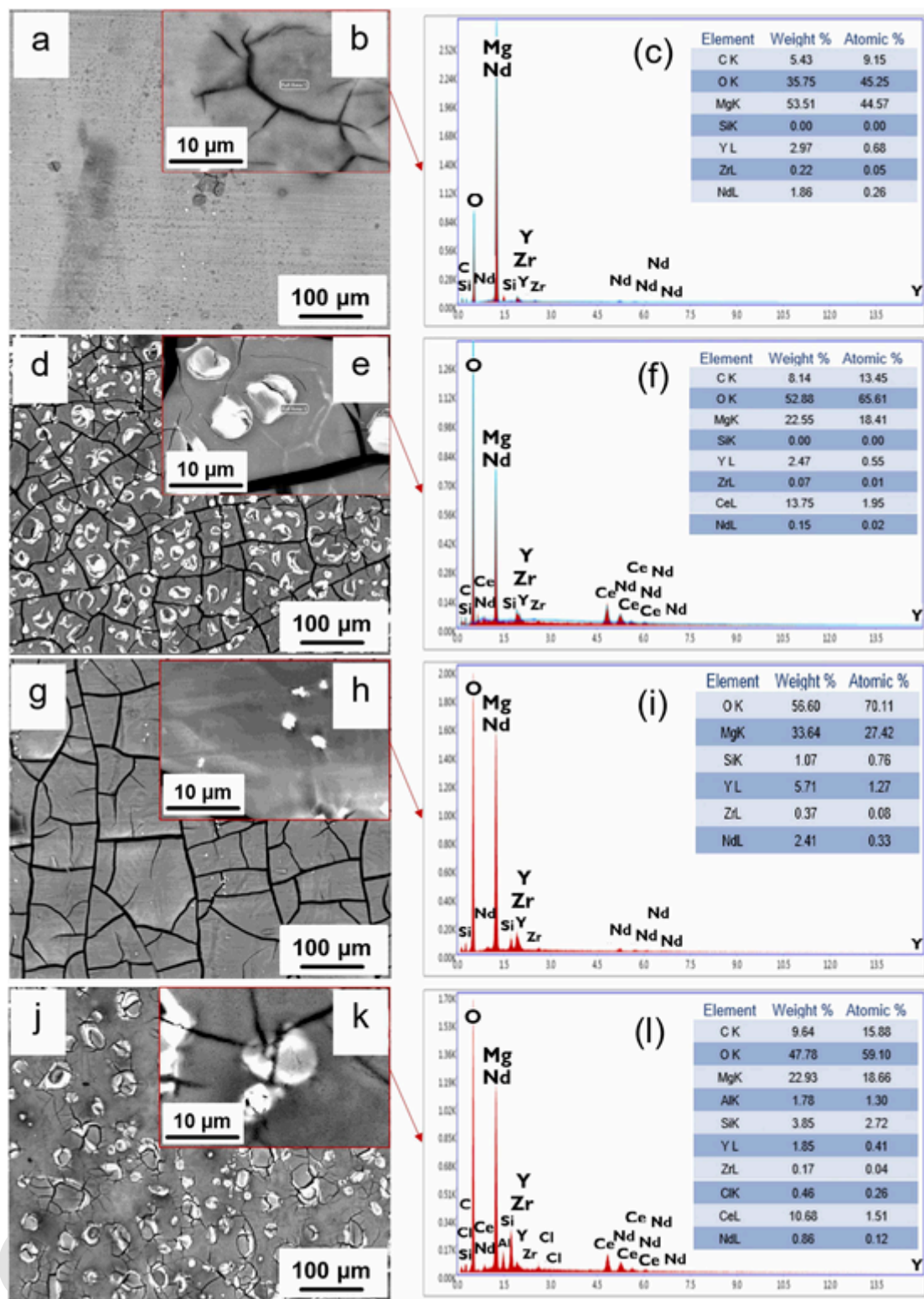
Fig. 11. SEM micrographs and EDS analyses obtained after the EIS test of (a-c) bare substrate, (d-f) cerium conversion coating (CEP), (g-i) hybrid sol-gel coating (Hyb), and (j-l) duplex CeP-Hyb coating on WE43-T5 substrate.

the other hand, the micrograph with higher definition (Fig. 11e) depicts a region with narrower cracks similar to that showed in Fig. 2c; some of them are filled with a white corrosion product, indicating oxide precipitation within these microstructural features. The Figures also display tiny white nodules regularly distributed all over the sample surface, which bright contrast indicates oxide precipitation (Fig. 11f). The comparison between the Mg/Ce ratios for the CeP sample prior (3.6) (Fig.

2d) and after (1.6) (Fig. 11f) the EIS tests show an important increase of the Ce amount in the corrosion product layer, indicating an important enrichment of Ce-rich species. However, the crack network must constitute conductive pathways for aggressive electrolyte penetration; therefore, the corrosion behavior of this sample was only slightly superior to the bare WE43 sample.

Table 3

Results of the fitting procedure of the EIS diagrams with the EEC of Fig. 8 for the WE43-T5 without coating and with the different coatings.

WE43-T5

Time (h)	Rs ($\Omega.cm^2$)	CPE-F (F.cm^{-2}.$s^{(n-1)}$)	n-F	Rct ($\Omega.cm^2$)	R-W ($\Omega.cm^2$)	n-W
1	67.2	1.73E-05	0.92	1820	1248	0.47
4	63.4	1.61E-05	0.93	2550	1652	0.44
6	61.7	1.59E-05	0.93	2915	1871	0.41
12	63.5	1.53E-05	0.93	4858	1926	0.42
18	65.7	1.56E-05	0.92	4926	1668	0.45
24	64.5	1.61E-05	0.92	3177	1645	0.42

CeP

Time (h)	Rs ($\Omega.cm^2$)	CPE-F (F.cm^{-2}.$s^{(n-1)}$)	n-F	Rct ($\Omega.cm^2$)	R-W ($\Omega.cm^2$)	n-W
1	71.3	1.63E-05	0.91	2060	1542	0.45
4	69.3	1.73E-05	0.92	4449	3277	0.41
6	69.8	1.77E-05	0.92	4989	3784	0.41
12	71.1	1.82E-05	0.91	5715	4270	0.39
18	71.3	1.88E-05	0.91	5768	4252	0.38
24	69.2	1.94E-05	0.91	4363	3574	0.40

Hyb

Time (h)	Rs + R_H ($\Omega.cm^2$)	CPE-F (F.cm^{-2}.$s^{(n-1)}$)	n-F	Rct ($\Omega.cm^2$)	R-W ($\Omega.cm^2$)	n-W
1	101.9	1.16E-06	0.89	9370	6586	0.39
4	149.1	1.36E-06	0.88	14,209	8460	0.47
6	148.2	1.46E-06	0.88	15,124	9103	0.48
12	148.5	1.66E-06	0.87	15,331	9086	0.50
18	147.5	1.91E-06	0.86	16,202	8755	0.52
24	141.9	2.07E-06	0.87	15,220	9009	0.48

CeP-Hyb

Time (h)	Rs + R_H ($\Omega.cm^2$)	CPE-F (F.cm^{-2}.$s^{(n-1)}$)	n-F	Rct ($\Omega.cm^2$)	R-W ($\Omega.cm^2$)	n-W
1	121.6	1.47E-06	0.79	12,780	10486	0.42
4	109.2	4.18E-06	0.75	16,600	8338	0.52
6	110.6	5.14E-06	0.74	20,968	8906	0.54
12	116.8	6.52E-06	0.75	26,501	8592	0.59
18	120.0	7.17E-06	0.77	26,911	8141	0.60
24	116.5	7.69E-06	0.79	22,485	7141	0.59

Fig. 11g and h show the surface morphology of the Hyb sample after the EIS tests. The corroded surface (Fig. 11g) shows a network of cracks, which origin has already been commented in the previous paragraph; however, no whitish spots were identified, and the micrograph at higher magnification (Fig. 11h) is smoother, differentiating the morphology of this corroded surface from the previously commented CeP sample. Comparing to the uncorroded sample (Fig. 2g), the chemical composition of the corroded surface (Fig. 11i) indicates incorporation of Y and Nd in the corrosion product layer and an important decrease in the Si content, thus showing that the hybrid layer is being damaged and leached by the test electrolyte. However, as indicated in the results of the electrochemical corrosion characterization, the coating is still effective for corrosion protection, contributing to better anticorrosive performance compared with the WE43-T5 and CeP samples. Finally, a qualitative comparison between the micrographs of Fig. 11g and d clearly show that the crack network is less dense when the hybrid layer is present, reducing the pathways for electrolyte penetration. This is in accordance with Nezamdoust et al. [53] findings, indicating that cracks may be sealed by the hybrid coating, contributing for the improved corrosion resistance.

The corroded surface of the CeP-Hyb sample after the EIS test is depicted in Fig. 11j and k. This sample displays a surface that can be better correlated with the as-prepared one (Fig. 2h), corroborating the increased anticorrosion performance demonstrated in the electrochemical corrosion tests. However, increasing in the density of cracked regions indicates electrolyte penetration, justifying the descending EIS modulus after 24 h (Fig. 10). The EDS characterization, displayed in Fig. 11l, shows smaller quantities of RE elements incorporated in the

corrosion product layer when compared with Fig. 11i, which is coherent with the higher thickness of the protective layer and minor degree of corrosion compared to the other samples. On the other hand, a higher quantity of Si was identified than for the corroded Hyb system, indicating that the hybrid coating is better preserved. Even though not explored in the present work, this particular result points to a positive interaction between the Ce conversion coating and the hybrid layer. This issue is being better studied with another protective system and will be subjected to publication shortly.

3.6. Physical model for the coated samples

The results of the fitting procedures showed that the whole set of EIS diagrams were fitted using a single EEC; therefore, the experimental impedance diagrams were not able to separate the contributions of the different coatings from that of the bare substrate. However, based on the results presented in Table 3 and in the cross-section analysis of the different coatings (Fig. 3), a physical model for the samples coated with the different systems could be proposed (Fig. 12), at which, as in Fig. 8, dotted lines were used to indicate possible existing current pathways not detected in the impedance experiments.

The results displayed in Table 3 showed an increase of HF resistance for the samples protected with the hybrid coating (Hyb and CeP-Hyb), indicating an increase in the resistive pathway. This response was associated with the resistance to penetration of the electrolyte through defective sites (pores) of the hybrid coating in series with R_s. As shown in several EIS fitting procedures of coated samples, the pore resistance (R_H in the present study) is frequently represented in parallel with the coating capacity [43,97,98]. However, in the present investigation, the meager pore resistance (tenths of Ohm.cm^2) precludes the EIS experiments to detect the hybrid coating [99], which, according to the cross-section micrographs displayed in Fig. 3b and c (thicknesses higher than 1 μm), must display a capacity value in the order of few nF.cm^{-2}. Therefore, in the high frequency limit (corresponding to the flat domain in the HF region of the impedance modulus plot, Fig. 7f and h), two series resistances were detected, and the current pathway corresponding to the hybrid layer capacity is represented by dotted lines (see Fig. 12b and c). On the other hand, the values of the CPE associated with the HF capacitive loop were about one order of magnitude lower for the hybrid coated samples. Taking into account the physical model presented in Fig. 8a, this response could be associated both to a thicker protective film leading to a lower (CPE-f) value and to the reduction of the bare Mg substrate exposed to the electrolyte through the defective sites of the protective film, resulting in a reduction of the double layer capacity (CPE-dl), this latter hypothesis is corroborated by the increase of Rct when the sample is protected with the hybrid coating.

Regarding the structure of the protective film, as previously discussed, the Mg oxide layer is composed of a thin protective film on top of which there is a porous non-protective layer [75,83]. For the Hyb and CeP-Hyb samples, it is proposed that percolation of the hybrid sol-gel coating through this porous layer (in the case of the CeP-Hyb sample also topped by a cracked Ce-conversion layer-see Fig. 3c) would take place, thus, increasing the total thickness of the protective layer and leading to a decrease of CPE-f. Therefore, the two phenomena (protective layer thickening and reduction of the bare substrate area exposed to the electrolyte) would result in a more protective system, as verified in the overall results of the present investigation. It is important to emphasize that the order of magnitude of the CPE determined for the HF capacitive loop for the Hyb and CeP-Hyb coatings (10^{-6} F.cm^{-2}.$s^{(n-1)}$) is not compatible with a thick protective layer, usually in the order of few micrometers, determined for sol-gel coatings (Fig. 3) [43,92], supporting the proposed physical model, at which the hybrid coating capacity (C_H) is represented as dotted lines, indicating that, even though presented at the metal surface, as proved by EDS analyses, it cannot be detected by the EIS measurements. On the other hand, for the sample pro-
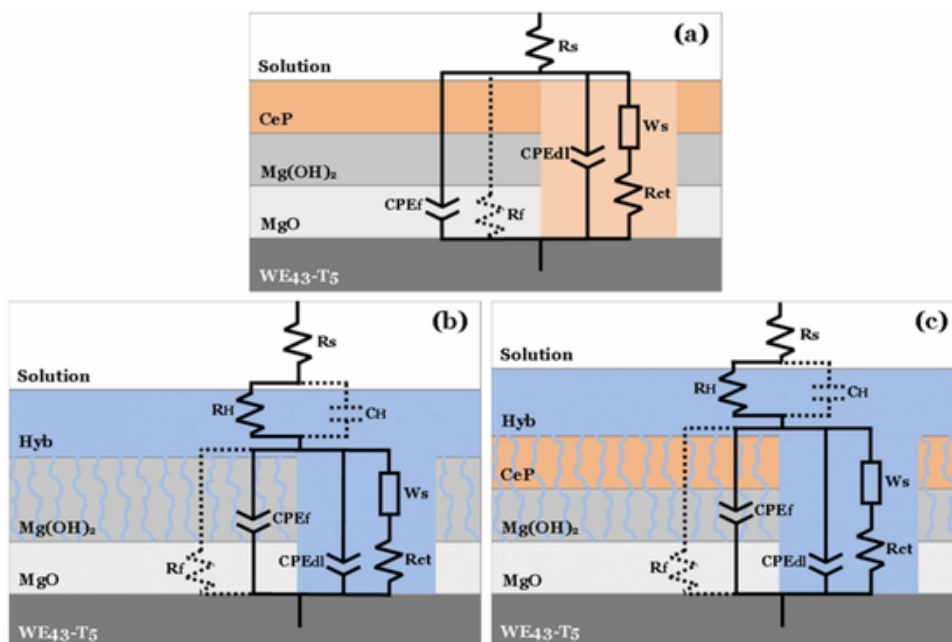
Fig. 12. Physical model for the different coating systems: (a) CeP, (b) Hyb, and (c) CeP-Hyb. Dotted lines were used to represent existing pathways through which current does not leak considering the corrosion resistance of the different systems and our experimental conditions. The thicknesses of the different layers are not in scale.

tected only with the Ce conversion coating, the cracked nature of this layer, associated with its low hydrophobicity [63,70,92] (Fig. 4b), would lead only to a slight increase in the corrosion resistance, as verified in the experimental results.

3.7. Local electrochemical impedance spectroscopy in the mapping mode (LEIM)

The active protection (self-healing) afforded by chromate-based inhibitors is a desirable feature to be exhibited by any corrosion protection system. In the literature, several authors reported self-healing properties for Ce-based protection systems [100,101], including for Mg alloys [102]. Fig. 13 displays the admittance LEIM diagrams of the Hyb (Fig. 13a, c, e, g) and CeP-Hyb (Fig. 13b, d, f, h) samples with an artificial defect immersed in NaCl 5 mM solution up to 24 h. For the Hyb sample, the anodic activity at the defective region, characterized by its high admittance modulus, is maintained and slightly grows until the end of the test, indicating increasing corrosion activity. Contrary, the corrosion activity on the CeP-Hyb sample is rapidly (Fig. 13d) and consistently reduced up to the end of the test, showing a progressive reduction of the electrochemical activity that can be associated with a self-healing effect. These results indicate that Ce ions released from the coating system can migrate to the defective sites, precipitating at regions with cathodic activity [26,27], thus hindering the continuity of the corrosion activity, as shown and discussed in the next paragraph. Fig. 14 displays the OM of the coated (Hyb and CeP-Hyb) samples with artificial defects after the LEIM tests for 24 h in NaCl 5 mM (a and b), and the SEM-EDS analysis of the defective region for the CeP-Hyb sample (c and d). Fig. 14a (Hyb) shows that the defective area is characterized by a dark color as a consequence of the corrosion process concentrated in this region, evidenced in the LEIM maps. In addition, despite the low aggressiveness of the test electrolyte, several round-shaped stains were identified in the nearby sample surface (some of them surrounded by red circles), indicating possible deterioration of the protective properties of the coating. On the other hand, for the CeP-Hyb sample (Fig. 14b), in accordance with the lowering of the corrosion activity with immersion time verified in the LEIM experiments, the defective region appears brighter; moreover, no sign of deterioration could be

observed in the vicinity of the analyzed area, indicating that the coating maintains its integrity. A magnified SEM micrograph, acquired after the completion of the LEIM test, of a selected region of the interior of the defect of the CeP-Hyb sample is depicted in Fig. 14c, whereas the EDS analysis of the selected area is shown in Fig. 14d. The micrograph shows the precipitation of white corrosion products inside the defect, which EDS analysis demonstrated to be Ce-rich oxides. The pattern of this deposit is completely different from that exhibited in the fresh produced samples (Fig. 2 c and d) or either of the corroded samples after the EIS experiments (Fig. 11), corroborating with the hypothesis that Ce ions released from the protective coating can precipitate at electrochemically active regions halting the corrosion activity in the defect [26,27,102]. Therefore, besides improving the overall corrosion resistance, as shown in the global electrochemical measurements, the presence of the Ce conversion layer underneath the hybrid layer in the duplex CeP-Hyb coating also imparts self-healing ability (active protection) to the coating system. In this sense, in this protection strategy, it is important that the Ce ions source remains isolated from the bulk electrolyte, avoiding the lixiviation of the major part of the corrosion inhibiting species to the solution, this role is guaranteed by the barrier imposed by the hybrid layer, an strategy already employed by other researchers in the protection of Al alloys [100,103].

4. Conclusions

The present work dealt with the corrosion behavior in a saline electrolyte of a cerium conversion coating (CeP), a hybrid sol-gel coating (Hyb), and a duplex CeP-Hyb coating deposited onto the WE43-T5 magnesium alloy. The bare artificially aged WE43 substrate was used as a reference for corrosion resistance. The results allowed for demonstrating the following:

I) The single treatment in $Ce(NO_3)_3 \cdot 6H_2O$ + 10 % v/v H_2O_2 aqueous solution does not significantly increase the corrosion resistance of the WE43-T5 Mg alloy, apparently due to the non-homogeneous surface microstructure of the cerium conversion layer generated, as shown by the SEM results.
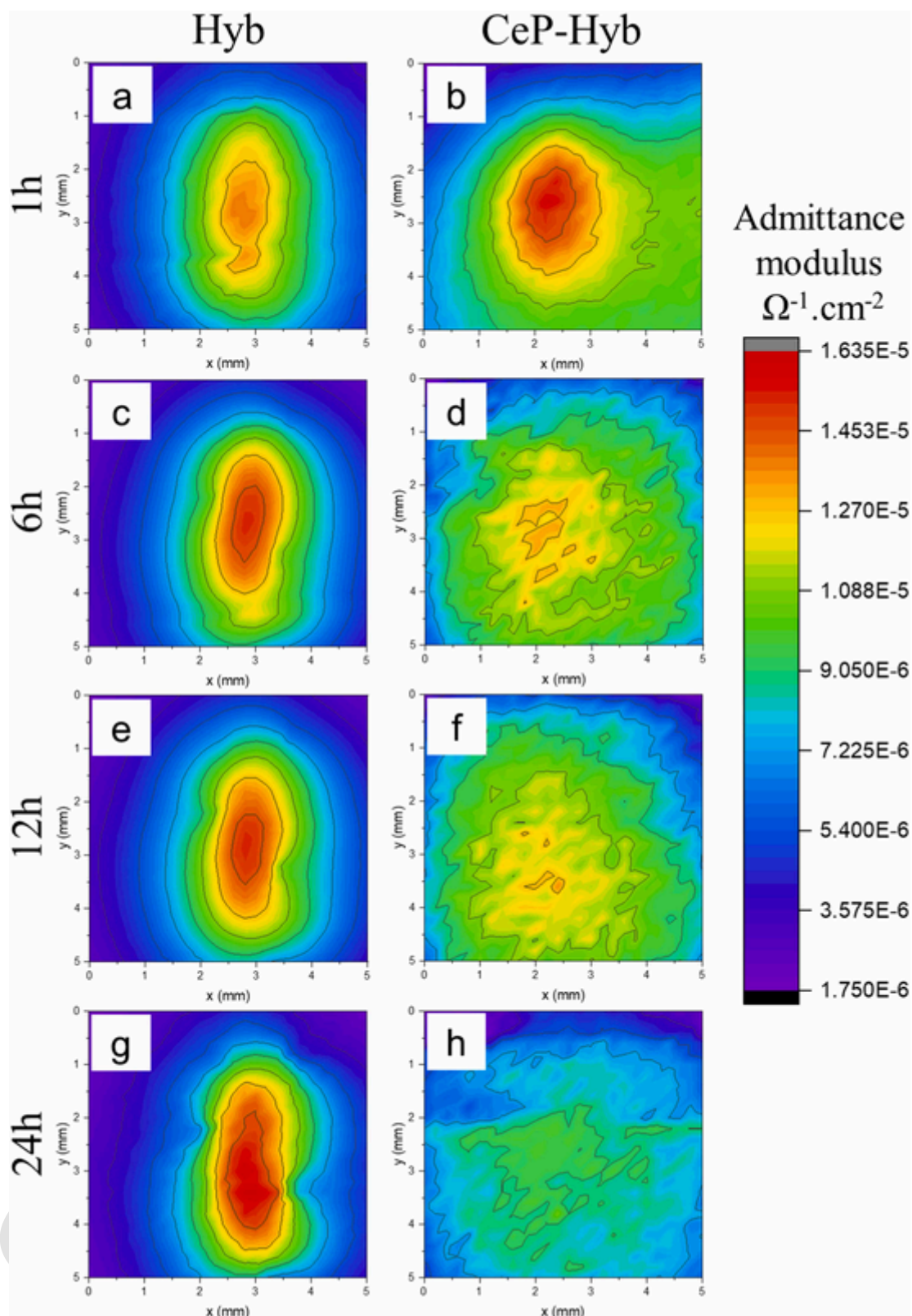
Fig. 13. LEIM diagrams of the WE43-T5 alloy coated with (a,c,e,g) Hyb and (b,d,f,h) CeP-Hyb. Coatings with an artificial defect.

II) The hybrid sol-gel coating deposition improves the corrosion protection of the WE43-T5 Mg alloy. Nevertheless, hydrogen evolution during the coating application generates defects that could decrease the effectiveness of the coating in long periods in contact with aggressive environments.

III) The addition of a cerium-based conversion layer before the hybrid sol-gel coating increases the corrosion protection of the protective system due to the more homogeneous surface morphology obtained compared to the single sol-gel coating, as demonstrated by AFM measurements of the as-produced coating and SEM micrographs of as-produced and corroded samples.
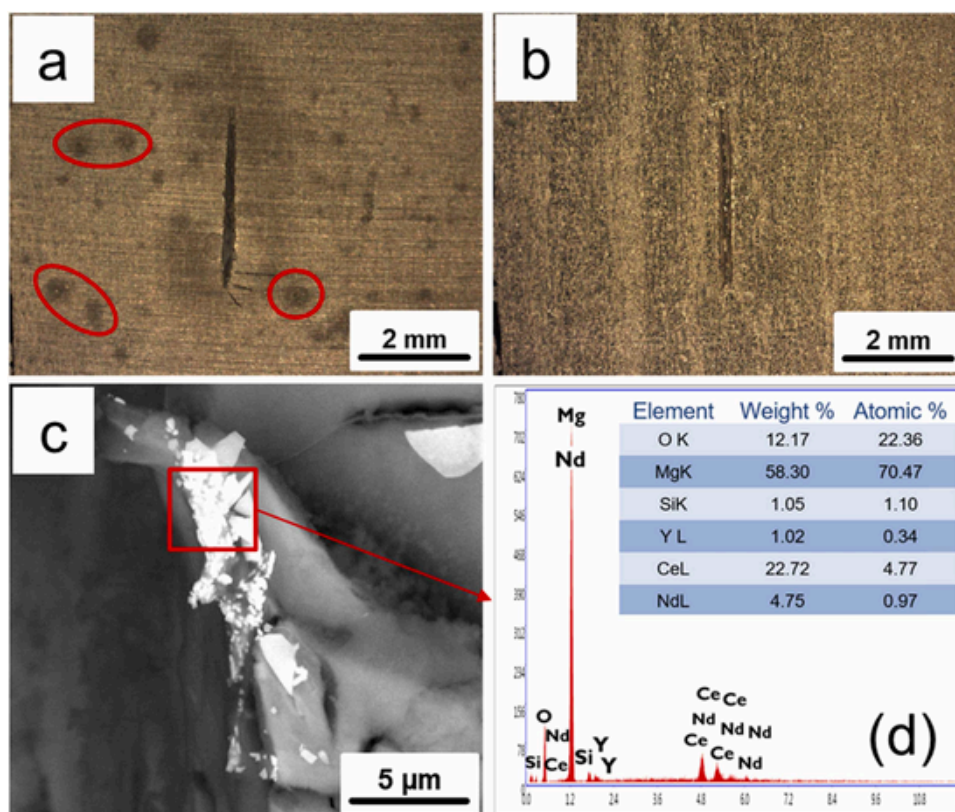
Element	Weight %	Atomic %
O K	12.17	22.36
MgK	58.30	70.47
SiK	1.05	1.10
Y L	1.02	0.34
CeL	22.72	4.77
NdL	4.75	0.97

Fig. 14. Optical micrographs of the artificial defects after the LEIM test for 24 h in NaCl 5 mM: (a) hybrid sol-gel sample (Hyb) and (b) duplex CeP-Hyb sample. (c) SEM micrographs and (d) EDS analysis of the interior of the defective region of the duplex CeP-Hyb sample after the LEIM test.

IV) LEIM experiments showed self-healing capabilities for the CeP-Hyb sample. Indicating that Ce species from the underlying conversion layer can migrate to defective sites and hinder the development of corrosion activity.

V) The results of the EEC fitting procedure revealed that, even though promising and protective, the produced surface treatment could be improved, aiming to enhance the barrier properties of the hybrid coating. This feature is being investigated and will be published shortly.

CRediT authorship contribution statement

Gualter Silva Pereira : Conceptualization, Data curation, Formal analysis, Funding acquisition, Supervision, Validation, Writing – original draft, Writing – review & editing. **Oscar Mauricio Prada Ramirez :** Conceptualization, Data curation, Formal analysis, Funding acquisition, Supervision, Validation, Writing – original draft, Writing – review & editing. **Pedro Renato Tavares Avila :** Conceptualization, Data curation, Formal analysis, Funding acquisition, Validation, Writing – original draft, Writing – review & editing. **Julian Arnaldo Avila Diaz :** Conceptualization, Formal analysis, Funding acquisition, Writing – review & editing. **Haroldo Cavalcanti Pinto :** Conceptualization, Formal analysis, Funding acquisition, Supervision, Validation, Writing – review & editing. **Marcos Hideki Miyazaki :** Conceptualization, Funding acquisition. **Hercílio Gomes de Melo :** Conceptualization, Data curation, Formal analysis, Funding acquisition, Supervision, Validation, Writing – review & editing. **Waldek Wladimir Bose Filho :** Conceptualization, Formal analysis, Funding acquisition, Supervision, Validation, Writing – review & editing.

Declaration of Competing Interest

The authors declare that they have no known competing financial interests or personal relationships that could have appeared to influence the work reported in this paper.

Data availability

Data will be made available on request..

Acknowledgments

Declaration of competing interest

The authors declare no conflict of interest.

Appendix A. Supporting information

Supplementary data associated with this article can be found in the online version at doi:10.1016/j.corsci.2022.110527.

References

[1] N.V. Murillo-Gutiérrez, F. Ansart, J.P. Bonino, M.J. Menu, M. Gressier, Protection against corrosion of magnesium alloys with both conversion layer and sol-gel coating, Surf. Coat. Technol. 232 (2013) 606–615, https://doi.org/10.1016/j.surfcoat.2013.06.036.

[2] X. Zhong, Q. Li, J. Hu, X. Yang, F. Luo, Y. Dai, Effect of cerium concentration on microstructure, morphology and corrosion resistance of cerium–silica hybrid coatings on magnesium alloy AZ91D, Prog. Org. Coat. 69 (2010) 52–56, https://doi.org/10.1016/j.porgcoat.2010.05.004.

[3] Z. Yang, J.P. Li, J.X. Zhang, G.W. Lorimer, J. Robson, Review on research and development of magnesium alloys, Acta Metall. Sin. 21 (2008) 313–328, https://doi.org/10.1016/S1006-7191(08)60054-X.

[4] J. Ninlachart, Z. Karmiol, D. Chidambaram, K.S. Raja, Effect of heat treatment conditions on the passivation behavior of WE43C Mg–Y–Nd alloy in chloride containing alkaline environments, J. Magnes. Alloy. 5 (2017) 147–165, https://doi.org/10.1016/j.jma.2017.03.003.

[5] S. You, Y. Huang, K.U. Kainer, N. Hort, Recent research and developments on wrought magnesium alloys, J. Magnes. Alloy. 5 (2017) 239–253, https://doi.org/10.1016/j.jma.2017.09.001.

[6] H. Liu, F. Cao, G.-L. Song, D. Zheng, Z. Shi, M.S. Dargusch, A. Atrens, Review of the atmospheric corrosion of magnesium alloys, J. Mater. Sci. Technol. 35 (2019) 2003–2016, https://doi.org/10.1016/j.jmst.2019.05.001.

[7] J. Song, J. She, D. Chen, F. Pan, Latest research advances on magnesium and magnesium alloys worldwide, J. Magnes. Alloy. 8 (2020) 1–41, https://doi.org/10.1016/j.jma.2020.02.003.

[8] G.S. Pereira, G.Y. Koga, J.A. Avila Diaz, I.M. Bittencourt, F. Fernandez, M.H. Miyazaki, W.J. Botta, W.W.Bose Filho, Corrosion resistance of WE43 Mg alloy in sodium chloride solution, Mater. Chem. Phys. 272 (2021) 124930, https://doi.org/10.1016/j.matchemphys.2021.124930.

[9] E.P. Silva, R.H. Buzolin, F. Marques, F. Soldera, U. Alfaro, H.C. Pinto, Effect of Ce-base mischmetal addition on the microstructure and mechanical properties of hot-rolled ZK60 alloy, J. Magnes. Alloy. 9 (2020) 995–1006, https://doi.org/10.1016/j.jma.2020.09.018.

[10] E.P. da Silva, R.H. Buzolin, U. Alfaro, G. Requena, H.C. Pinto, Microstructure and mechanical behavior of similar butt-joints of ZK60 and ZK60–1.5RE magnesium alloys produced by linear friction stir welding, J. Magnes. Alloy (2021), https://doi.org/10.1016/j.jma.2021.04.012.

[11] J.H. Chu, L.B. Tong, Z.H. Jiang, D.N. Zou, Q.J. Wang, S.F. Liu, H.J. Zhang, A comparison study of Ce/La and Ca microalloying on the bio-corrosion behaviors of extruded Mg-Zn alloys, J. Magnes. Alloy. 8 (2020) 1269–1280, https://doi.org/10.1016/j.jma.2019.09.011.

[12] C. Xiang, N. Gupta, P. Coelho, K. Cho, Effect of microstructure on tensile and compressive behavior of WE43 alloy in as cast and heat treated conditions, Mater. Sci. Eng. A. 710 (2018) 74–85, https://doi.org/10.1016/j.msea.2017.10.084.

[13] S. Ghorbanpour, B.A. McWilliams, M. Knezevic, Low-cycle fatigue behavior of rolled WE43-T5 magnesium alloy, Fatigue Fract. Eng. Mater. Struct. 42 (2019) 1357–1372, https://doi.org/10.1111/ffe.12992.

[14] E. Bütev Öcal, Z. Esen, K. Aydınol, A.F. Dericioğlu, Comparison of the short and long-term degradation behaviors of as-cast pure Mg, AZ91 and WE43 alloys, Mater. Chem. Phys. 241 (2020) 122350, https://doi.org/10.1016/j.matchemphys.2019.122350.

[15] B. Milkereit, L. Burgschat, R.H. Kemsies, A. Springer, C. Schick, O. Kessler, In situ differential scanning calorimetry analysis of dissolution and precipitation kinetics in Mg–Y–RE alloy WE43, J. Magnes. Alloy. 7 (2019) 1–14, https://doi.org/10.1016/j.jma.2019.01.002.

[16] N. Li, C. Guo, Y.H. Wu, Y.F. Zheng, L.Q. Ruan, Comparative study on corrosion behaviour of pure Mg and WE43 alloy in static, stirring and flowing Hank's solution, Corros. Eng. Sci. Technol. 47 (2012) 346–351, https://doi.org/10.1179/1743278212Y.0000000006.

[17] M. Jahedi, B.A. McWilliams, M. Knezevic, Deformation and fracture mechanisms in WE43 magnesium-rare earth alloy fabricated by direct-chill casting and rolling, Mater. Sci. Eng. A 726 (2018) 194–207, https://doi.org/10.1016/j.msea.2018.04.090.

[18] E.A. Lukyanova, N.S. Martynenko, V.N. Serebryany, A.N. Belyakov, L.L. Rokhlin, S.V. Dobatkin, Y.Z. Estrin, Structure and mechanical and corrosion properties of a magnesium Mg–Y–Nd–Zr alloy after high pressure torsion, Russ. Metall. 2017 (2017) 912–921, https://doi.org/10.1134/S0036029517110088.

[19] M. Esmaily, J.E. Svensson, S. Fajardo, N. Birbilis, G.S. Frankel, S. Virtanen, R. Arrabal, S. Thomas, L.G. Johansson, Fundamentals and advances in magnesium alloy corrosion, Prog. Mater. Sci. 89 (2017) 92–193, https://doi.org/10.1016/j.pmatsci.2017.04.011.

[20] J.E. Gray, B. Luan, Protective coatings on magnesium and its alloys – a critical review, J. Alloy. Compd. 336 (2002) 88–113, https://doi.org/10.1016/S0925-8388(01)01899-0.

[21] V.S. Saji, Review of rare-earth-based conversion coatings for magnesium and its alloys, J. Mater. Res. Technol. 8 (2019) 5012–5035, https://doi.org/10.1016/j.jmrt.2019.08.013.

[22] D. Wang, G.P. Bierwagen, Sol–gel coatings on metals for corrosion protection, Prog. Org. Coat. 64 (2009) 327–338, https://doi.org/10.1016/j.porgcoat.2008.08.010.

[23] X.-B. Chen, M.A. Easton, N. Birbilis, H.-Y. Yang, T.B. Abbott, Corrosion-resistant coatings for magnesium (Mg) alloys, in: Corrosion Prevention of Magnesium Alloys, Elsevier, 2013, pp. 282–312, https://doi.org/10.1533/9780857098962.2.282.

[24] M.L. Zheludkevich, D.G. Shchukin, K.A. Yasakau, M.G.S. Ferreira, Anticorrosion Coatings with Self-Healing Effect Based on Nanocontainers Impregnated with Corrosion Inhibitor, 100 (2007) 402–411, https://doi.org/10.1021/cm062066k.

[25] Q. Li, Sol-gel coatings to improve the corrosion resistance of magnesium (Mg) alloys, in: Corrosion Prevention of Magnesium Alloys, Elsevier, 2013, pp. 469–485, https://doi.org/10.1533/9780857098962.3.469.

[26] B.R.W. Hinton, Corrosion inhibition with rare earth metal salts, J. Alloy. Compd. 180 (1992) 15–25, https://doi.org/10.1016/0925-8388(92)90359-H.

[27] B.R.W. Hinton, D.R. Arnott, N.E. Ryan, Inhibition of aluminum alloy corrosion by cerous cations, Met. Forum 7 (1984) 211–217.

[28] M. Terada, F.M. Queiroz, D.B.S. Aguiar, V.H. Ayusso, H. Costenaro, M.-G. Olivier, H.G. de Melo, I. Costa, Corrosion resistance of tartaric-sulfuric acid anodized AA2024-T3 sealed with Ce and protected with hybrid sol–gel coating, Surf. Coat. Technol. 372 (2019) 422–426, https://doi.org/10.1016/j.surfcoat.2019.05.028.

[29] R. del Olmo, U. Tiringer, I. Milošev, P. Visser, R. Arrabal, E. Matykina, J.M.C. Mol, Hybrid sol-gel coatings applied on anodized AA2024-T3 for active corrosion protection, Surf. Coat. Technol. 419 (2021) 127251, https://doi.org/10.1016/j.surfcoat.2021.127251.

[30] S. Sun, D. Li, D. Liu, B. Yang, Y. Ren, J. Liu, H. Xie, Effects of Bi and Ce addition on tensile properties and corrosion resistance of Zn-15Al alloys by continuous casting and extrusion, Mater. Lett. 275 (2020) 128027, https://doi.org/10.1016/j.matlet.2020.128027.

[31] R. Raj, M.G. Taryba, Y. Morozov, R. Kahraman, R.A. Shakoor, M.F. Montemor, On the synergistic corrosion inhibition and polymer healing effects of polyolefin coatings modified with Ce-loaded hydroxyapatite particles applied on steel, Electrochim. Acta 388 (2021) 138648, https://doi.org/10.1016/j.electacta.2021.138648.

[32] X. Li, S. Deng, Ce(SO4)2 as an efficient corrosion inhibitor for cold rolled steel in citric acid solution, J. Taiwan Inst. Chem. Eng. 122 (2021) 273–283, https://doi.org/10.1016/j.jtice.2021.04.057.

[33] C.S. Lin, S.K. Fang, Formation of cerium conversion coatings on AZ31 magnesium alloys, J. Electrochem. Soc. 152 (2005) B54, https://doi.org/10.1149/1.1845371.

[34] A.L. Rudd, C.B. Breslin, F. Mansfeld, The corrosion protection afforded by rare earth conversion coatings applied to magnesium, Corros. Sci. 42 (2000) 275–288, https://doi.org/10.1016/S0010-938X(99)00076-1.

[35] T. Takenaka, T. Ono, Y. Narazaki, Y. Naka, M. Kawakami, Improvement of corrosion resistance of magnesium metal by rare earth elements, Electrochim. Acta 53 (2007) 117–121, https://doi.org/10.1016/j.electacta.2007.03.027.

[36] C.E. Castano, M.J. O'Keefe, W.G. Fahrenholtz, Microstructural evolution of cerium-based coatings on AZ31 magnesium alloys, Surf. Coat. Technol. 246 (2014) 77–84, https://doi.org/10.1016/j.surfcoat.2014.03.010.

[37] L. LI, J. LEI, S. YU, Y. TIAN, Q. JIANG, F. PAN, Formation and characterization of cerium conversion coatings on magnesium alloy, J. Rare Earths 26 (2008) 383–387, https://doi.org/10.1016/S1002-0721(08)60101-5.

[38] M.F. Montemor, A.M. Simões, M.G.S. Ferreira, M.J. Carmezim, Composition and corrosion resistance of cerium conversion films on the AZ31 magnesium alloy and its relation to the salt anion, Appl. Surf. Sci. 254 (2008) 1806–1814, https://doi.org/10.1016/j.apsusc.2007.07.187.

[39] X. Cui, Y. Yang, E. Liu, G. Jin, J. Zhong, Q. Li, Corrosion behaviors in physiological solution of cerium conversion coatings on AZ31 magnesium alloy, Appl. Surf. Sci. 257 (2011) 9703–9709, https://doi.org/10.1016/j.apsusc.2011.04.141.

[40] S. Ben Hassen, L. Bousselmi, P. Berçot, M. El Rezrazi, E. Triki, XPS characterization and corrosion resistance of cerium-treated magnesium coatings, Rare Met. 30 (2011) 368–373, https://doi.org/10.1007/s12598-011-0398-y.

[41] S. Zhang, Q. Li, B. Chen, X. Yang, Preparation and corrosion resistance studies of nanometric sol–gel-based CeO2 film with a chromium-free pretreatment on AZ91D magnesium alloy, Electrochim. Acta 55 (2010) 870–877, https://doi.org/10.1016/j.electacta.2009.07.053.

[42] V. Dalmoro, D.S. Azambuja, C. Alemán, E. Armelin, Hybrid organophosphonic-silane coating for corrosion protection of magnesium alloy AZ91: The influence of acid and alkali pre-treatments, Surf. Coat. Technol. 357 (2019) 728–739, https://doi.org/10.1016/j.surfcoat.2018.10.013.

[43] S.V. Lamaka, M.F. Montemor, A.F. Galio, M.L. Zheludkevich, C. Trindade, L.F. Dick, M.G.S. Ferreira, Novel hybrid sol – gel coatings for corrosion protection of AZ31B magnesium alloy, 53 (2008) 4773–4783. https://doi.org/10.1016/j.electacta.2008.02.015.

[44] E. Bakhshandeh, A. Jannesari, Z. Ranjbar, S. Sobhani, M.R. Saeb, Anti-corrosion hybrid coatings based on epoxy–silica nano-composites: toward relationship between the morphology and EIS data, Prog. Org. Coat. 77 (2014) 1169–1183, https://doi.org/10.1016/j.porgcoat.2014.04.005.

[45] P.S. Correa, C.F. Malfatti, D.S. Azambuja, Corrosion behavior study of AZ91 magnesium alloy coated with methyltriethoxysilane doped with cerium ions, Prog. Org. Coat. 72 (2011) 739–747, https://doi.org/10.1016/j.porgcoat.2011.08.005.

[46] W.J. van Ooij, D. Zhu, V. Palanivel, J.A. Lamar, M. Stacy, Overview: the potential of silanes for chromate replacement in metal finishing industries, Silicon Chem. 3 (2006) 11–30, https://doi.org/10.1007/s11201-005-4407-6.

[47] D. Zhu, W.J. van Ooij, Corrosion protection of AA 2024-T3 by bis-[3-(triethoxysilyl)propyl]tetrasulfide in sodium chloride solution, Corros. Sci. 45 (2003) 2177–2197, https://doi.org/10.1016/S0010-938X(03)00061-1.

[48] M. Mrad, Y. Ben Amor, L. Dhouibi, M.F. Montemor, Effect of AA2024-T3 surface pretreatment on the physicochemical properties and the anticorrosion performance of poly(γ-glycidoxypropyltrimethoxysilane) sol-gel coating, Surf.

Interface Anal. 50 (2018) 335–345, https://doi.org/10.1002/sia.6373.

[49] M. Bestetti, A. Da Forno, P.L. Cavallotti, P. Gronchi, F. Barlassina, Anodic oxidation and sol–gel coatings for corrosion and wear protection of AM60B alloy, Trans. IMF 88 (2010) 57–62, https://doi.org/10.1179/174591909X12596814696567.

[50] A.L.K. Tan, A.M. Soutar, I.F. Annergren, Y.N. Liu, Multilayer sol–gel coatings for corrosion protection of magnesium, Surf. Coat. Technol. 198 (2005) 478–482, https://doi.org/10.1016/j.surfcoat.2004.10.066.

[51] A.N. Khramov, V.N. Balbyshev, L.S. Kasten, R.A. Mantz, Sol–gel coatings with phosphonate functionalities for surface modification of magnesium alloys, Thin Solid Films 514 (2006) 174–181, https://doi.org/10.1016/j.tsf.2006.02.023.

[52] R. Pinto, M.J. Carmezim, M.G.S. Ferreira, M.F. Montemor, A two-step surface treatment, combining anodisation and silanisation, for improved corrosion protection of the Mg alloy WE54, Prog. Org. Coat. 69 (2010) 143–149, https://doi.org/10.1016/j.porgcoat.2010.04.014.

[53] S. Nezamdoust, D. Seifzadeh, Application of Ce – V / sol – gel composite coating for corrosion protection of AM60B magnesium alloy, Trans. Nonferrous Met. Soc. China 27 (2017) 352–362, https://doi.org/10.1016/S1003-6326(17)60039-6.

[54] ASTM B661-12, Standard practice for heat treatment of magnesium alloys, ASTM Int. 12 (2012) 1–7, https://doi.org/10.1520/B0661-12R20.2.

[55] O.M. Prada Ramirez, F.M. Queiroz, M. Terada, U. Donatus, I. Costa, M.-G. Olivier, H.G. de Melo, EIS investigation of a Ce-based posttreatment step on the corrosion behaviour of Alclad AA2024 anodized in TSA, Surf. Interface Anal. (2019), https://doi.org/10.1002/sia.6633.

[56] O.M. Prada Ramirez, F.M. Queiroz, M.A. Tunes, R.A. Antunes, C.L. Rodrigues, A. Lanzutti, S. Pogatscher, M.-G. Olivier, H.G.De Melo, Tartaric-sulphuric acid anodized clad AA2024-T3 post-treated in Ce-containing solutions at different temperatures: corrosion behaviour and Ce ions distribution, Appl. Surf. Sci. 534 (2020) 147634, https://doi.org/10.1016/j.apsusc.2020.147634.

[57] O.M. Prada Ramirez, M.A. Tunes, M.M. Mennucci, M. Starykevich, C. Neves, M.G.S. Ferreira, S. Pogatscher, H.G.De Melo, Ce post-treatment for increased corrosion resistance of AA2024-T3 anodized in tartaric-sulfuric acid, Corros. Sci. 204 (2022) 110371, https://doi.org/10.1016/j.corsci.2022.110371.

[58] K.S. Durán, N. Hernández, L.M. Rueda, C.A. Hernández-Barrios, A.E. Coy, F. Viejo, Design of multilayer hybrid sol-gel coatings with bifunctional barrier-bioactive response on the Elektron 21 magnesium alloy for biomedical applications, J. Magnes. Alloy. 9 (2021) 2097–2112, https://doi.org/10.1016/j.jma.2021.03.020.

[59] H. Ashassi-Sorkhabi, S. Moradi-Alavian, R. Jafari, A. Kazempour, E. Asghari, Effect of amino acids and montmorillonite nanoparticles on improving the corrosion protection characteristics of hybrid sol-gel coating applied on AZ91 Mg alloy, Mater. Chem. Phys. 225 (2019) 298–308, https://doi.org/10.1016/j.matchemphys.2018.12.059.

[60] C.A. Hernández-Barrios, C.A. Cuao, M.A. Jaimes, A.E. Coy, F. Viejo, Effect of the catalyst concentration, the immersion time and the aging time on the morphology, composition and corrosion performance of TEOS-GPTMS sol-gel coatings deposited on the AZ31 magnesium alloy, Surf. Coat. Technol. 325 (2017) 257–269, https://doi.org/10.1016/j.surfcoat.2017.06.047.

[61] V. Krishnan, T. Lakshmi, Bioglass: a novel biocompatible innovation, J. Adv. Pharm. Technol. Res. 4 (2013) 78–83, https://doi.org/10.4103/2231-4040.111523.

[62] A.S. Nguyen, N. Pébère, Electrochimica Acta A local electrochemical impedance study of the self-healing properties of waterborne coatings on 2024 aluminium alloy, Electrochim. Acta 222 (2016) 1806–1817, https://doi.org/10.1016/j.electacta.2016.11.152.

[63] Y. Reyes, A. Durán, Y. Castro, Glass-like cerium sol-gel coatings on AZ31B magnesium alloy for controlling the biodegradation of temporary implants, Surf. Coat. Technol. 307 (2016) 574–582, https://doi.org/10.1016/j.surfcoat.2016.09.056.

[64] S.J. Hinder, R. Grilli, M. Rustame, W.I.A. Santos, M.A. Baker, I. Costa, A surface analytical investigation of cerium-based conversion coatings deposited onto an AA2024-T3 aluminium alloy cladding layer, Surf. Interface Anal. 46 (2014) 735–739, https://doi.org/10.1002/sia.5440.

[65] X. Liu, M. Wang, H. Li, L. Wang, Y. Xu, Electrochemical effects of pH value on the corrosion inhibition and microstructure of cerium doped trivalent chromium conversion coating on Zn, Corros. Sci. 167 (2020) 108538, https://doi.org/10.1016/j.corsci.2020.108538.

[66] S. Nezamdoust, D. Seifzadeh, Z. Rajabalizadeh, Application of novel sol–gel composites on magnesium alloy, J. Magnes. Alloy. 7 (2019) 419–432, https://doi.org/10.1016/j.jma.2019.03.004.

[67] W. Yao, W. Liang, G. Huang, B. Jiang, A. Atrens, F. Pan, Superhydrophobic coatings for corrosion protection of magnesium alloys, J. Mater. Sci. Technol. 52 (2020) 100–118, https://doi.org/10.1016/j.jmst.2020.02.055.

[68] H. Zhou, J. Li, J. Li, Q. Ruan, X. Peng, S. Li, W. Jin, Z. Yu, P.K. Chu, W. Li, A composite coating with physical interlocking and chemical bonding on WE43 magnesium alloy for corrosion protection and cytocompatibility enhancement, Surf. Coat. Technol. 412 (2021) 127078, https://doi.org/10.1016/j.surfcoat.2021.127078.

[69] S. Heise, T. Wirth, M. Höhlinger, Y.T. Hernández, J.A.R. Ortiz, V. Wagener, S. Virtanen, A.R. Boccaccini, Electrophoretic deposition of chitosan/bioactive glass/silica coatings on stainless steel and WE43 Mg alloy substrates, Surf. Coat. Technol. 344 (2018) 553–563, https://doi.org/10.1016/j.surfcoat.2018.03.050.

[70] E. Saei, B. Ramezanzadeh, R. Amini, M.S. Kalajahi, Effects of combined organic and inorganic corrosion inhibitors on the nanostructure cerium based conversion coating performance on AZ31 magnesium alloy: morphological and corrosion studies, Corros. Sci. 127 (2017) 186–200, https://doi.org/10.1016/j.corsci.2017.08.017.

[71] S. Roshan, A.A. Sarabi, Improved performance of Ti-based conversion coating in the presence of Ce/Co ions: surface characterization, electrochemical and adhesion study, Surf. Coat. Technol. 410 (2021) 126931, https://doi.org/10.1016/j.surfcoat.2021.126931.

[72] J. Drábiková, S. Fintová, P. Ptáček, I. Kuběna, M. Březina, J. Wasserbauer, P. Doležal, F. Pastorek, Structure and growth kinetic of unconventional fluoride conversion coating prepared on wrought AZ61 magnesium alloy, Surf. Coat. Technol. 399 (2020) 126101, https://doi.org/10.1016/j.surfcoat.2020.126101.

[73] G.S. Frankel, A. Samaniego, N. Birbilis, Evolution of hydrogen at dissolving magnesium surfaces, Corros. Sci. 70 (2013) 104–111, https://doi.org/10.1016/j.corsci.2013.01.017.

[74] C.P. de Abreu, I. Costa, H.G. de Melo, N. Pébère, V. Vivier, B. Tribollet, Multiscale electrochemical study of welded Al alloys joined by friction stir welding, J. Electrochem. Soc. 164 (2017) C735–C746, https://doi.org/10.1149/2.0391713jes.

[75] G. Baril, G. Galicia, C. Deslouis, N. Pébère, B. Tribollet, V. Vivier, An impedance investigation of the mechanism of pure magnesium corrosion in sodium sulfate solutions, J. Electrochem. Soc. 154 (2007) C108, https://doi.org/10.1149/1.2401056.

[76] J. Liu, Y. Song, J. Chen, P. Chen, D. Shan, E.H. Han, The special role of anodic second phases in the micro-galvanic corrosion of EW75 Mg alloy, Electrochim. Acta 189 (2016) 190–195, https://doi.org/10.1016/j.electacta.2015.12.075.

[77] V.B. Oliveira, L.R. Viera, B. de, A. Lima, P.R.T. Avila, G.C. Rêgo, H.C. Pinto, I.N. Bastos, E.P. da Silva, Corrosion behavior of as-cast ZK60 alloy modified with rare earth addition in sodium sulfate medium, Corros. Sci. 158 (2019), https://doi.org/10.1016/j.corsci.2019.108092.

[78] P.W. Chu, E.A. Marquis, Linking the microstructure of a heat-treated WE43 Mg alloy with its corrosion behavior, Corros. Sci. 101 (2015) 94–104, https://doi.org/10.1016/j.corsci.2015.09.005.

[79] S. Fajardo, C.F. Glover, G. Williams, G.S. Frankel, The source of anodic hydrogen evolution on ultra high purity magnesium, Electrochim. Acta 212 (2016) 510–521, https://doi.org/10.1016/j.electacta.2016.07.018.

[80] Z. Shi, J.X. Jia, A. Atrens, Galvanostatic anodic polarization curves and galvanic corrosion of AZ31B in 0.01 M Na 2SO 4 saturated with Mg(OH) 2, Adv. Eng. Mater. 14 (2012) 324–334, https://doi.org/10.1002/adem.201100257.

[81] M.L. White, H. Vedage, R.D. Granate, H. Leidheiser, Failure mechanisms for organic coatings subjected to 0.1 M sulfuric acid, Ind. Eng. Chem. Prod. Res. Dev. 25 (1986) 129–132, https://doi.org/10.1021/i300022a001.

[82] G. Baril, C. Blanc, N. Pébère, AC impedance spectroscopy in characterizing time-dependent corrosion of AZ91 and AM50 magnesium alloys characterization with respect to their microstructures, J. Electrochem. Soc. 148 (2001) B489, https://doi.org/10.1149/1.1415722.

[83] S. Leleu, B. Rives, J. Bour, N. Causse, N. Pébère, On the stability of the oxides film formed on a magnesium alloy containing rare-earth elements, Electrochim. Acta 290 (2018) 586–594, https://doi.org/10.1016/j.electacta.2018.08.093.

[84] L. Wang, D. Snihirova, M. Deng, C. Wang, B. Vaghefinazari, G. Wiese, M. Langridge, D. Höche, S.V. Lamaka, M.L. Zheludkevich, Insight into physical interpretation of high frequency time constant in electrochemical impedance spectra of Mg, Corros. Sci. 187 (2021) 109501, https://doi.org/10.1016/j.corsci.2021.109501.

[85] M. del, R. Silva Campos, C. Blawert, C.L. Mendis, M. Mohedano, T. Zimmermann, D. Proefrock, M.L. Zheludkevich, K.U. Kainer, Effect of heat treatment on the corrosion behavior of Mg-10Gd alloy in 0.5% NaCl solution, Front. Mater. 7 (2020), https://doi.org/10.3389/fmats.2020.00084.

[86] G. Baril, N. Pébère, The corrosion of pure magnesium in aerated and deaerated sodium sulphate solutions, Corros. Sci. 43 (2001) 471–484, https://doi.org/10.1016/S0010-938X(00)00095-0.

[87] M.P. Gomes, I. Costa, N. Pébère, J.L. Rossi, B. Tribollet, V. Vivier, On the corrosion mechanism of Mg investigated by electrochemical impedance spectroscopy, Electrochim. Acta 306 (2019) 61–70, https://doi.org/10.1016/j.electacta.2019.03.080.

[88] I. Epelboin, M. Keddam, O.R. Mattos, H. Takenouti, The dissolution and passivation of Fe and Fe-Cr alloys in acidified sulphate medium: influences of pH and Cr content, Corros. Sci. 19 (1979) 1105–1112, https://doi.org/10.1016/S0010-938X(79)80099-2.

[89] I.V. Aoki, M.C. Bernard, S.I.C. De Torresi, C. Deslouis, H.G. De Melo, S. Joiret, B. Tribollet, Ac-impedance and Raman spectroscopy study of the electrochemical behaviour of pure aluminum in citric acid media, Electrochim. Acta 46 (2001) 1871–1878, https://doi.org/10.1016/S0013-4686(01)00431-5.

[90] H. Xiong, K. Yu, X. Yin, Y. Dai, Y. Yan, H. Zhu, Effects of microstructure on the electrochemical discharge behavior of Mg-6wt%Al-1wt%Sn alloy as anode for Mg-air primary battery, J. Alloy. Compd. 708 (2017) 652–661, https://doi.org/10.1016/j.jallcom.2016.12.172.

[91] M. Guan, Y. Hu, T. Zheng, T. Zhao, F. Pan, Composition optimization and mechanical properties of Mg-Al-Sn-Mn alloys by orthogonal design, Materials 11 (2018), https://doi.org/10.3390/ma11081424.

[92] C.A. Hernández-Barrios, J.A. Saavedra, S.L. Higuera, A.E. Coy, F. Viejo, Effect of cerium on the physicochemical and anticorrosive features of TEOS-GPTMS sol-gel coatings deposited on the AZ31 magnesium alloy, Surf. Interfaces 21 (2020), https://doi.org/10.1016/j.surfin.2020.100671.

[93] B. Hirschorn, M.E. Orazem, B. Tribollet, V. Vivier, I. Frateur, M. Musiani, Determination of effective capacitance and film thickness from constant-phase-element parameters, Electrochim. Acta 55 (2010) 6218–6227, https://doi.org/10.1016/j.electacta.2009.10.065.

[94] X. Jiang, R. Guo, S. Jiang, Evaluation of self-healing ability of Ce–V conversion coating on AZ31 magnesium alloy, J. Magnes. Alloy. 4 (2016) 230–241, https://doi.org/10.1016/j.jma.2016.06.003.

[95] J. Xie, J. Zhang, Z. You, S. Liu, K. Guan, R. Wu, J. Wang, J. Feng, Towards developing Mg alloys with simultaneously improved strength and corrosion resistance via RE alloying, J. Magnes. Alloy. 9 (2021) 41–56, https://doi.org/10.1016/j.jma.2020.08.016.

[96] F. Rosalbino, E. Angelini, S. De Negri, A. Saccone, S. Delfino, Effect of erbium addition on the corrosion behaviour of Mg-A1 alloys, Intermetallics 13 (2005) 55–60, https://doi.org/10.1016/j.intermet.2004.05.007.

[97] A. Trentin, A. de, L. Gasparini, F.A. Faria, S.V. Harb, F.C. dos Santos, S.H. Pulcinelli, C.V. Santilli, P. Hammer, Barrier properties of high performance PMMA-silica anticorrosion coatings, Prog. Org. Coat. 138 (2020) 105398, https://doi.org/10.1016/j.porgcoat.2019.105398.

[98] A.A. El hadad, F.R. García-Galván, M.A. Mezour, G.J. Hickman, I.E. Soliman, A. Jiménez-Morales, V. Barranco, J.C. Galván, C.C. Perry, Organic-inorganic hybrid coatings containing phosphorus precursors prepared by sol–gel on Ti6Al4V alloy: Electrochemical and in-vitro biocompatibility evaluation, Prog. Org. Coat. 148 (2020) 105834, https://doi.org/10.1016/j.porgcoat.2020.105834.

[99] M.E. Orazem, B. Tribollet, Electrochemical Impedance Spectroscopy, John Wiley & Sons, Inc., Hoboken, NJ, USA, 2008, https://doi.org/10.1002/9780470381588.

[100] L.M. Palomino, P.H. Suegama, I.V. Aoki, M.F. Montemor, H.G. De Melo, Electrochemical study of modified cerium-silane bi-layer on Al alloy 2024-T3, Corros. Sci. 51 (2009) 1238–1250, https://doi.org/10.1016/j.corsci.2009.03.012.

[101] G. Yoganandan, K.P. Premkumar, J.N. Balaraju, Evaluation of corrosion resistance and self-healing behavior of zirconium – cerium conversion coating developed on AA2024 alloy, Surf. Coat. Technol. 270 (2015) 249–258, https://doi.org/10.1016/j.surfcoat.2015.02.049.

[102] S.Y. Jian, C.Y. Yang, J.K. Chang, Robust corrosion resistance and self-healing characteristics of a novel Ce / Mn conversion coatings on EV31 magnesium alloys, Appl. Surf. Sci. 510 (2020) 145385, https://doi.org/10.1016/j.apsusc.2020.145385.

[103] N.C. Rosero-Navarro, L. Paussa, F. Andreatta, Y. Castro, A. Durán, M. Aparicio, L. Fedrizzi, Optimization of hybrid sol-gel coatings by combination of layers with complementary properties for corrosion protection of AA2024, Prog. Org. Coat. 69 (2010) 167–174, https://doi.org/10.1016/j.porgcoat.2010.04.013.